NEAR-FIELD SCANNING MICROWAVE MICROSCOPY OF SUPERCONDUCTING MICROSTRIP RESONATORS

by

Ashfaq S. Thanawalla

Dissertation submitted to the Faculty of the Graduate School of the
University of Maryland, College Park in partial fulfillment
of the requirements for the degree of
Doctor of Philosophy
2000

Advisory Committee:

Associate Professor Frederick C. Wellstood, Chair/Advisor
Associate Professor Steven M. Anlage
Professor Richard L. Greene
Professor Christopher J. Lobb
Assistant Professor Ichiro Takeuchi

ABSTRACT

Title of Dissertation: NEAR-FIELD SCANNING MICROWAVE MICROSCOPY OF SUPERCONDUCTING MICROSTRIP RESONATORS

Ashfaq S. Thanawalla, Doctor of Philosophy, 2000

Dissertation directed by: Associate Professor Frederick C. Wellstood
Department of Physics

I describe the operation of a cryogenic near-field scanning microwave microscope which uses an open-ended coaxial cable to image electric field distributions near superconducting devices. The microscope operates in the frequency range from 0.01 to 20 GHz. The system uses an open-ended coaxial probe with the inner and outer conductor made of copper and the dielectric material in between made of teflon. The diameter of the inner conductor is 200 μm, and this determines the spatial resolution of the microscope. The operating temperature of the microscope is 77 K to 300 K though, in principle, it could be cooled down to liquid Helium temperatures. I have used the microscope to image electric field distributions and intermodulation fields from a $Tl_2Ba_2CaCu_2O_8$ (TBCCO) superconducting microstrip resonator. The resonator has a

650-nm-thick film of TBCCO deposited on both sides of a 420-μm-thick, 4.7 mm X 9.9 mm MgO substrate. One side serves as a ground plane, while the other is patterned into a strip with a width of 150 mm and a length L = 7.1 mm. The resonant frequency of the resonator is 8.205 GHz. Images from the sample show clear evidence for perturbation of the electric field by the probe. Using a frequency following technique, I was able to map out the effect of the probe perturbation on the microstrip's resonant frequency.

NEAR-FIELD SCANNING MICROWAVE MICROSCOPY OF SUPERCONDUCTING MICROSTRIP RESONATORS

by

Ashfaq S. Thanawalla

Dissertation submitted to the Faculty of the Graduate School of the
University of Maryland, College Park in partial fulfillment
of the requirements for the degree of
Doctor of Philosophy
2000

Advisory Committee:

Associate Professor Frederick C. Wellstood, Chair/Advisor
Associate Professor Steven M. Anlage
Professor Richard L. Greene
Professor Christopher J. Lobb
Assistant Professor Ichiro Takeuchi

Dedication

To my parents

ACKNOWLEDGMENTS

I would like to thank a number of people who have helped me a great deal. First and foremost I would like to acknowledge my adviser Professor Frederick C. Wellstood in whose lab I worked on the Cryogenic Near-Field Scanning Microwave Microscope. My sincere appreciation goes to Dr. Wellstood for his guidance, patience and support without which I would not have been able to complete this thesis work. Dr. Wellstood's noble character will always be an inspiration to me. I gratefully acknowledge the patience, advice and support of Professor Steven M. Anlage. I sincerely thank Dr. Anlage for introducing me to near-field scanning microwave microscope.

In addition, I owe a great deal to those I worked closest with. I would like to thank Dr. Johan B. Feenstra for his patience, critical advice and good physical insight. I would like to thank my co-workers: Wensheng Hu for side by side laboring on the intermodulation experiments; Constantine Vlahacos, with whom I had interesting conversations about many things, and not just physics; Sojiphong Chatraphorn, who always found time from his own busy research schedule to help me countless times; Mark Gubrud and Matthew E. Kenyon for all the interesting and thoughtful discussion about philosophy; Erin F. Fleet and David E. Steinhauer for providing great company at the APS March meetings. I thank Sudeep K. Dutta for all his work on the microwave microscope and for his friendship.

I thank Profs. F. C. Wellstood, Steven M. Anlage, Richard L. Greene, Christopher J. Lobb and Ichiro Takeuchi for scheduling my thesis defense. I also thank Profs. Wellstood and Anlage for letters of recommendation.

I would like to thank all those who helped me assemble my microscope: Russ Wood, Mark Vilas, Jesse Anderson, all from the machine shop. I would like to acknowledge the people in the Electronics Development Group (EDG), Jack Touart and the late Ernie Knouse for all their time, patience and getting all things electrical working. I would like to thank Mark Giddings in the student shop for teaching me how to work the machines and for helpful suggestions. I would like to thank Doug Benson, Brian Straughn, Dawn Leavell, Belta Pollard, Grace Sewlall and Lisa Belcourt, all from the Center for their help in keeping track of paperwork and getting things done.

I thank my parents for a lifetime of encouragement and supporting my decision to pursue a Ph. D. in the U. S; my brother Afzal and his family for their friendship; a fervent thanks to my newer friends over the past ten years: Sanjay Kodiyalam for being a role model, Sanjay Khare and Alpan Raval for providing spiritual insights, Lubna Rana for interesting company, Krishnendu Sengupta for interesting conversations, Andrew Berkley for help with doctoral defense presentation.

TABLE OF CONTENTS

LIST OF FIGURES

Chapter 1

Introduction

1.1 Motivation

The discovery of high temperature superconductivity in 1986 by J. G. Bednorz and K. A. Muller [1] created real hope of finding new applications for superconductors in the everyday world. As I write this 14 years later, there is now belief that high-T_c superconducting (HTS) microwave devices may soon be the first to fulfill the promise of relatively abundant everyday applications of superconductors. The main application would be as filters in cellular base stations [2,3]. However, the use of HTS materials in these applications is predicated on their ability to retain a linear response under a variety of operating conditions. So far, this has turned out to be a significant impediment. The main motivation behind my thesis is to investigate a new route to understand and eventually control the microscopic causes of nonlinearity in HTS microwave devices.

1.2 Nonlinearity in superconductors

Microwave non-linearity in superconducting devices is manifested by the fact that the device response is not linear in the input power. Examples of such manifestations of non-linearity in band-pass filters include widening of the pass-band frequency range, and increased insertion loss as the power increases. For high-Q resonators, non-linearity manifests itself as a reduction of the quality factor (Q) [4], and shift in the resonant frequency [5] with power. Other effects of non-linearity come from frequency

conversion, and include intermodulation of two or more signals in the pass band of a filter [6], or harmonic generation in wideband devices such as delay lines.

1.3 Measurements of nonlinearity

All of these manifestations of nonlinearity can be traced to the fact that the electrodynamic properties of a superconductor are fundamentally non-linear. For a review of the electrodynamics of superconductors, see reference [7]. One direct measure of non-linearity is how the surface impedance Z_s depends on rf power. Ideally, one expects that Z_s is independent of the power.

Resonant techniques are often employed to measure the surface impedance of superconductors. Non-linearity often shows up first as changes in the resonator transmission response as a function of frequency. The surface resistance can be deduced from measurements of the Q of the resonator, while the surface reactance is found from measurements of the frequency shift of the resonator. It is generally found that the surface resistance and reactance tends to increase as higher microwave power is applied, i.e. the surface becomes more dissipative and more inductive as power increases. The surface resistance and reactance are generally observed to increase quadratically with rf field strength, H_{rf}, over a range of rf powers. Beyond a critical rf field strength, the increase is faster than quadratic, possibly indicating heating or a breakdown associated with the superconducting-to-normal-state transition.

This type of surface impedance measurement has the disadvantage that it is a global measurement and one must make the assumption that the material is homogeneous. In reality only a few areas of the film may be dominating the losses. Thus

a relatively homogeneous film with a few defective areas may be judged equivalent to a homogeneously degraded film.

A somewhat more sensitive measure of non-linearity can be obtained through measurements of harmonic generation in HTS devices. In this method, a signal at frequency f_1 is applied to the device. If the device is time reversal symmetric (i. e. no trapped flux or dc bias is present) then the I-V curve must obey the condition V(-I) = -V(I). If this is the case, then only odd harmonic terms can arise from non-linearities in the I-V curve of the device. To characterize the non-linear response, one usually measures the first (f_1) and the third ($3f_1$) harmonics exiting the device as a function of the input power at frequency f_1. Typically, it is found that with increasing field strength, harmonic generation and intermodulation will appear before one observes a change in the surface impedance. A significant disadvantage of this technique is the need to create a broadband device, or measurement system, which can characterize the sample at both the fundamental and third harmonic frequencies. In addition, one cannot obtain a spatially resolved measure of where or how the harmonics are generated.

Perhaps the smartest way to overcome the bandwidth problem is to use an intermodulation measurement technique. This technique also has the advantage of simulating common real-world communication problems associated with non-linearity: the mixing of two or more signals to create phantom signals in the same band. In this technique, two signals at frequencies f_1 and f_2 are applied to the device, both within the passband of the device. Typically one chooses the difference frequency $\Delta f = f_1 - f_2$ to be much less than the device band-width, but large enough to be outside the wings of any phase noise associated with the sources of the primary signals. A third order non-linearity will generate harmonics at frequencies $2f_1-f_2$ and $2f_2-f_1$ (among others), which are Δf

below f_1 and Δf above f_2, respectively. Since all the signals are within the device bandwidth, no special broadband design is necessary. With a cubic non-linearity, as the power in the primary signals is increased, the power observed in the third harmonic signals generally increases three times as fast. Although this characterization technique is convenient and directly relevant to such things as filter applications, it suffers once again from being a global or "black box" technique. In other words conventional intermodulation simply describes the overall nonlinearity and does not reveal local root causes of the problem.

1.4 Scanning probe microscopy

While optical microscopy is used in practically every branch of science and engineering, it is interesting to note that it only makes use of a narrow band of the electromagnetic spectrum, mainly in the visible. The longer-wavelength regime of the electromagnetic spectrum has largely been inaccessible by microscopic techniques. For finding sources of microwave non-linearity, a microscope that worked in the microwave band would clearly be technologically useful. However, obtaining microscopic images at long wavelengths poses certain challenges.

For example, the spatial resolution of a conventional optical microscope is limited by the classical Abbe diffraction limit [8] to approximately $\lambda/2$, where λ is the wavelength of the radiation used. This limit affects conventional optical systems ranging from astronomical telescopes to your eyes. The Abbe limit arises from the behavior of light propagating over distances much greater than a wavelength. This region is known as the "far field" and diffraction effects play a key role.

The possibility of sub-diffraction limit resolution was first recognized by Synge [9] in 1928. He proposed that a small (sub-wavelength) aperture could be used to light a spot that was smaller than the wavelength. This technique took off in 1980's with the invention of modern scanning-probe microscopy by Gerd Binning and Heinrich Rorher who invented the STM [10], and in 1986 received the Nobel Prize in Physics for their work. Many SPMs have followed since the inception of the STM, including:

(1) The atomic-force microscope (AFM) [11, 12]: sensitive to the force between a sample and an atomically sharp tip.

(2) The near-field scanning optical microscope (NSOM) [13, 14]. The NSOM uses a coated fiber optic transmission line that is tapered to an extremely fine tip at one end. Only the very end of the fiber optic line is left uncoated with metal to serve as a sub-wavelength aperture approximately 50-100 nm in diameter.

(3) Magnetic-force microscopes (MFM): measures the magnetic force from a sample by means of a sharp magnetic tip. Although their typical field sensitivity of a few hundred gauss is somewhat poor, MFMs can have a spatial resolution as low as about 0.025 μm [15, 16].

The essential feature of all scanning-probe microscopes is that the probe is in the near-field of the sample. The high spatial resolution is achieved by using a very sharp probe and scanning the probe very close to the surface to take advantage of the strong spatial dependence of the interaction at close range.

1.5 Microscopic imaging

In an effort to discover the origins of non-linearity and inhomogeneity in HTS materials, I have helped to develop a microscopic microwave-imaging technique. I have applied this technique to image operating device structures in order to begin to understand their high power properties. Several other groups have demonstrated electric field [17, 18] and magnetic field [19] imaging above operating microwave devices using near-field techniques. In addition, some groups have developed (far field) scanning laser [20, 21] and electron microscopes [22] which can image microwave currents on the few μm length scale. Image from such systems can form the basis for investigating the interaction of the microwave currents with the microstructure of the materials making up the device.

As I will describe beginning in Chapter 2, my microscope can be used to image electric and magnetic fields in the vicinity of operating microwave devices. The microscope detects the normal component of electric field, i.e. the electric field integrated over the exposed area of the center conductor of the probe. The spatial resolution is limited by the larger of the probe-sample separation and the size of the probe tip. As I will discuss throughout this thesis, there are a large number of technical issues which need to be addressed before we can exploit these microscopes to their fullest potential. As I will discuss in Chapter 4, one big problem is that there are perturbations of the device fields due to the presence of the measurement probe. This perturbation may be so large as to significantly change the frequency response and obscure the actual behavior of the fields. A second issue concerns the challenge of simultaneously obtaining the required spatial resolution, low temperature operation, and imaging capability on an operating superconducting microwave device. Finally, the probe-sample interaction is difficult to

accurately model, so that image interpretation and quantitative understanding can be difficult to obtain.

1.6 Outline of thesis

This thesis describes my work on the development of a cryogenic near-field microscope that operates at microwave frequencies.

In Chapter 2, I describe the design and basic operation of my cryogenic near-field scanning microwave microscope. Finally, I discuss the basic transmission line model for the system, the microscopes spatial resolution and the two basic modes of operation for the microscope.

In Chapter 3, I describe the scanning of a fine open-ended coaxial probe above an operating microwave device, and show images of local electric fields generated by the device at microwave frequencies. This work was carried out by myself, Constantine Vlahacos, Sudeep Dutta and Dr. Johan Feenstra. Using a simple model of the microscope, we are able to interpret the system's output and determine the magnitude of the electric field at the probe tip. In this chapter, I also show images of the electric field above a copper microstrip resonator and a superconducting microstrip resonator.

The presence of the measurement probe itself causes perturbations in the device response and the fields around the device. This perturbation may be so great as to noticeably change the device response. This is particularly true for high-Q devices. In Chapter 4, I describe how I first detected this effect in my system and how I used a frequency-following circuit to study and correct for the influence of the probe on the resonant frequency of the microstrip resonator.

Probably the most sensitive experimental characterization of superconducting nonlinearity is through intermodulation distortion (IMD) of two nearby pure tones. Intermodulation is also a practical measurement because it simulates the undesirable generation of ghost signals in a communication bandpass filter. Chapter 5 describes my imaging efforts on this important quantity in TBCCO superconducting filters. This work was carried out by myself, Wensheng Hu and Johan Feenstra.

Chapter 2

A cryogenic near-field scanning microwave microscope

2.1 Introduction

My research on microwave microscopy was made possible largely because of the considerable amount of prior work that has been done at the University of Maryland on novel scanning probe microscopes. In fact, my system is in many ways a descendant of the first one-dimensional SQUID microscope (designed and developed by Anna Mathai) [1] and two two-dimensional SQUID microscopes (designed and developed by Anna Mathai and Randall C. Black) [2]. These microscopes were used by Randy, Anna, and others in the group to image a wide variety of things, including,

1. Vertical component B_z of the magnetic field above a wire bent into a meander pattern and carrying a current [3].

2. Ferromagnetic ink on a bank check [3].

3. Magnetic ink on a U. S. one dollar Federal Reserve note [4].

4. Paramagnetic $Cd_{0.9}Mn_{0.1}Se$ in an applied magnetic field [5].

5. 50 kHz eddy-current in copper squares of different thickness patterned onto a printed circuit board at 77K [6].

6. 50 MHz field generated by an rf current in a loop.

7. The phase of the order parameter in YBCO [7, 8].

The next step in the evolution of the scanning SQUID microscope was the development of a microscope to image room-temperature samples in air. This microscope was primarily built by Randall C. Black in collaboration with Yonggyu Gim and Steven

M. Green at Neocera. My own microwave system uses a version of the scanning control software written by Randall C. Black for this SQUID system. A great deal of subsequent development has been done on the system by Erin F. Fleet and Sojiphong Chatraphorn.

Shortly after Randall C. Black and Yonggyu Gim completed the room temperature system, Constantine (Gus) P. Vlahacos assembled a benchtop microwave microscope. It is interesting to note that Gus started by building the drive stage for the new SQUID microscope and duplicated it for use in the new microwave scanner. Gus used the microwave system to image:

1. A microwave breadboard assembly [9].
2. A U.S. quarter dollar coin [10].
3. The topography of an etched glass chip [11].

Microwave microscopy was further developed by David E. Steinhauer. David built another room-temperature scanner and used it to image a wide variety of phenomenon, including:

1. Thin-film Cr lines on a NIST Resolution Target [12].
2. Microwave sheet resistance of a $YBa_2Cu_3O_{7-\delta}$ thin film [13].
3. High resolution dielectrics [14].
4. Nonlinear dielectrics [14].
5. Domains in ferroelectric crystals [15].
6. Critical Phenomena in Deuterated Triglycine Sulfate [14].

2.2 Design of the microscope

My work on microwave microscopy at cryogenic temperatures is a technical culmination of much of the previous microscopy efforts. The mechanical and cryogenic design of my microwave microscope is based on the two-dimensional SQUID microscope designed by Randall C. Black and Anna Mathai. The basic idea is that we have a cryogenic positioning mechanism that allows us to move a small probe closely over a cryogenic sample. My microscope produces 2-D images and allows for in situ sensor-sample control and sample temperature control.

The system which I use is based directly on Anna Mathai's cryogenic SQUID scanner. The system was built at the University of Cincinnati and was originally intended as a replacement for her system. I adapted it to its present use as a scanning microwave microscope.

Figure 2.1 shows an overall schematic of my cryogenic microwave microscope. A room-temperature part and a cold part together constitute the scanner (See Fig. 2.2 and Fig 2.3). The sample and the coaxial probe are contained in the cold part. The vacuum feedthroughs that control the sample position and the probe-sample separation constitute the room-temperature part. Long, thin-walled stainless steel tubes connect the two parts. Two pushrods which control the sample x-y motion are moved using rotary-to-linear motion vacuum feedthroughs. These feedthroughs are coupled to stepper motors via timing belts. The motors are rigidly mounted to the top of the dewar.

The cryogenic end of the push rods are connected to a delrin and teflon X-Y-Z translation stage. This stage was adapted from one originally designed by Randall C. Black and uses a slider box and wedges to control the sample

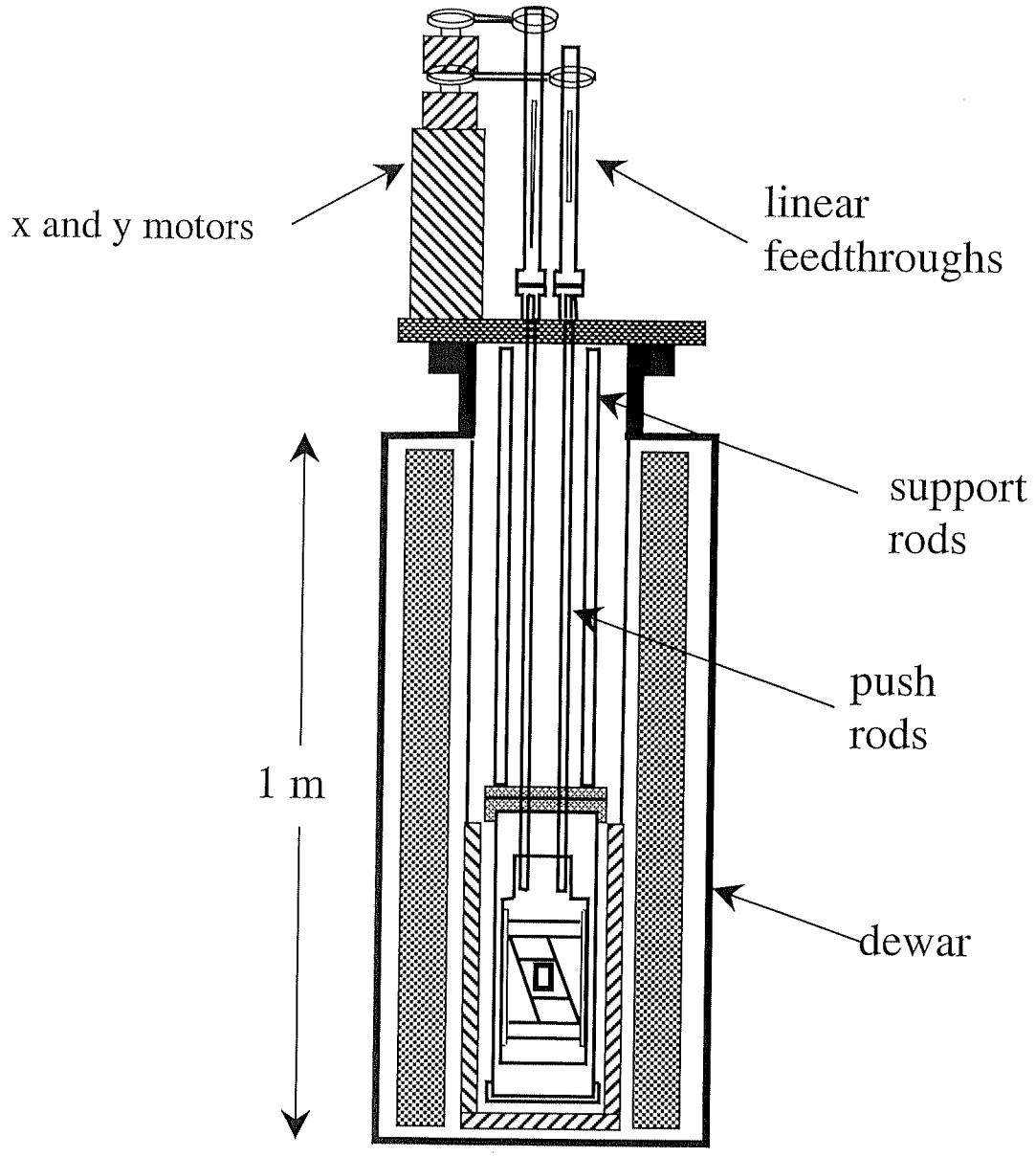

Fig. 2.1 Overall configuration of the 2-D microwave microscope, including the scanner, vacuum feedthroughs, dewar, motors, and computer.

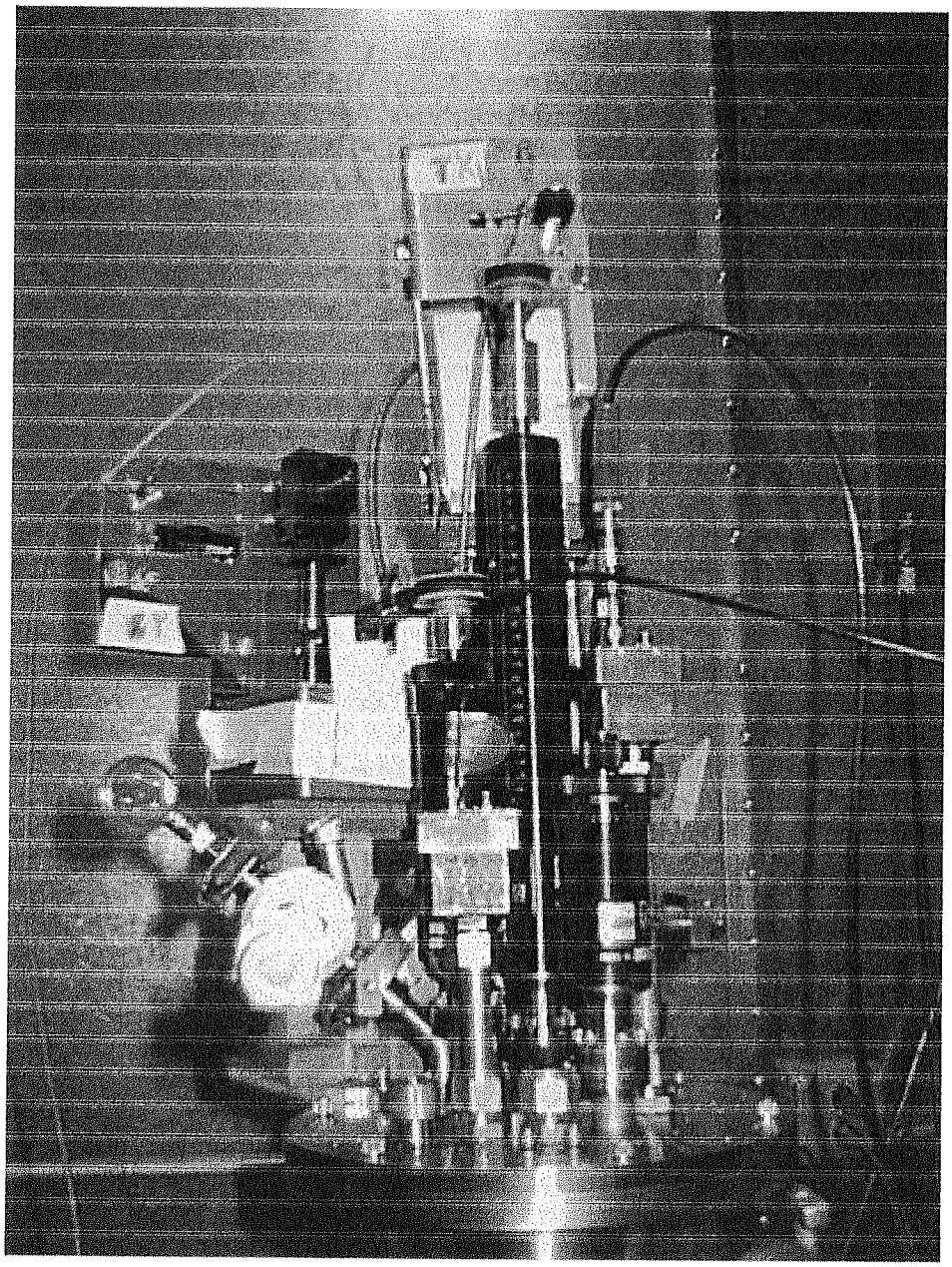

Fig. 2.2. Photograph of the top flange of the cryogenic microwave microscope

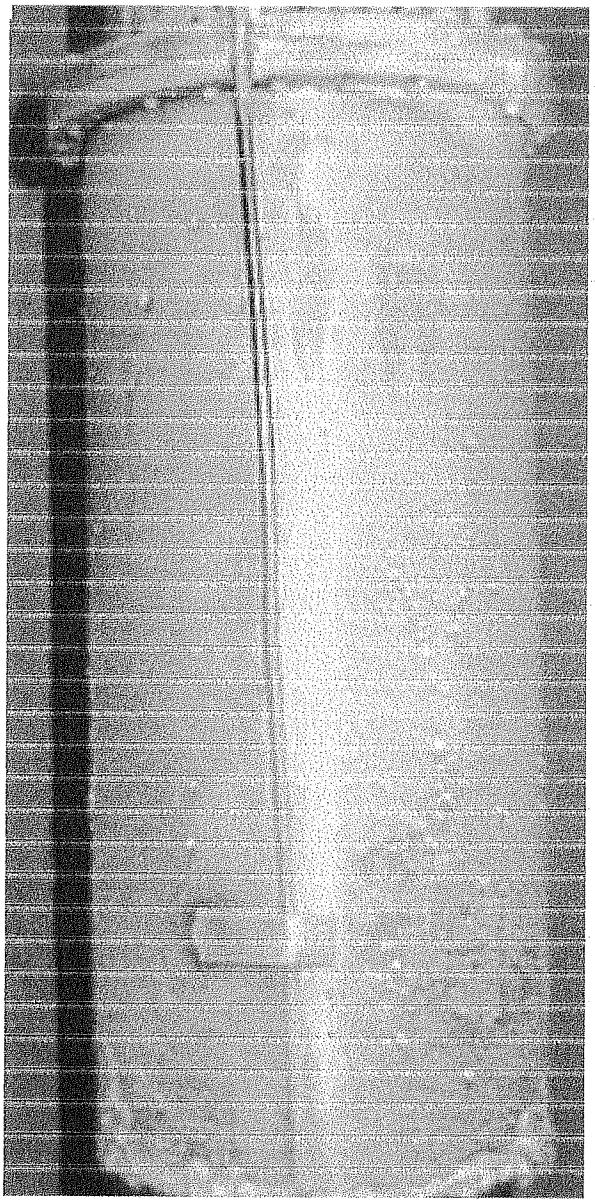

Fig. 2.3. Photograph of the cold flange of the microwave microscope when closed.

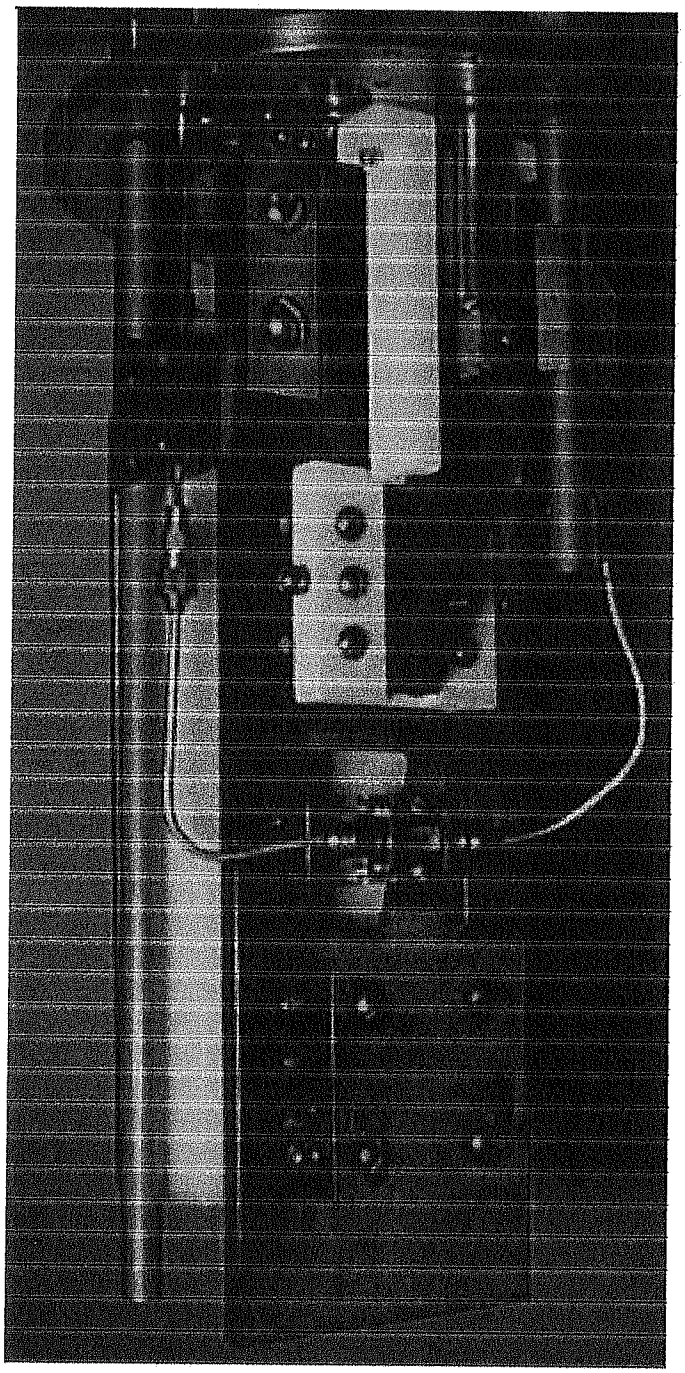

Fig. 2.4. Photograph of the front of the cold flange of the cryogenic microwave microscope.

motion (see next section). The sample is mounted on a small holder that allows fine control of the tilt and separation by the means of 3 screws.

The probe is held by a similar mount which faces the sample. After the probe and sample are leveled with respect to the scanning plane, I use an optical microscope to adjust the z-separation.

The cryogenic stage is enclosed in a vacuum can and is placed in a dewar which is filled with liquid nitrogen to cool the cold stage to 77 K during normal operation. A Gateway 2000 PC controls the motors and the data-acquisition.

2.2.1 The two-dimensional mechanism of the cold stage

The plan and front view of the cold stage of the scanner are shown in Figure 2.5.

The system has three interlocking sliders. The internal slider is parallelopiped in shape. There is a rectangular hole through its center. The piece of teflon which holds the sample goes in through this central hole and is attached to the back of the internal slider via bolts. The top and bottom surfaces of the internal slider are horizontal, and its left and right sides are approximately 15 degrees to the vertical. The top and bottom surfaces of the internal slider has horizontal grooves. Slider 1 consists of top and bottom components which are bolted together to fit within these grooves, thus creating a horizontal slot in which the internal slider can move to the left and right. Slider 1 rides on vertical teflon rails as it moves up and down and the internal slider and sample are moved with it. Slider 2 has 15 degree grooves along which the internal slider can move, thus constraining the motion of the internal slider by this slot and the horizontal slot.

In order to move the sample up or down during scanning, both sliders 1 and 2 are

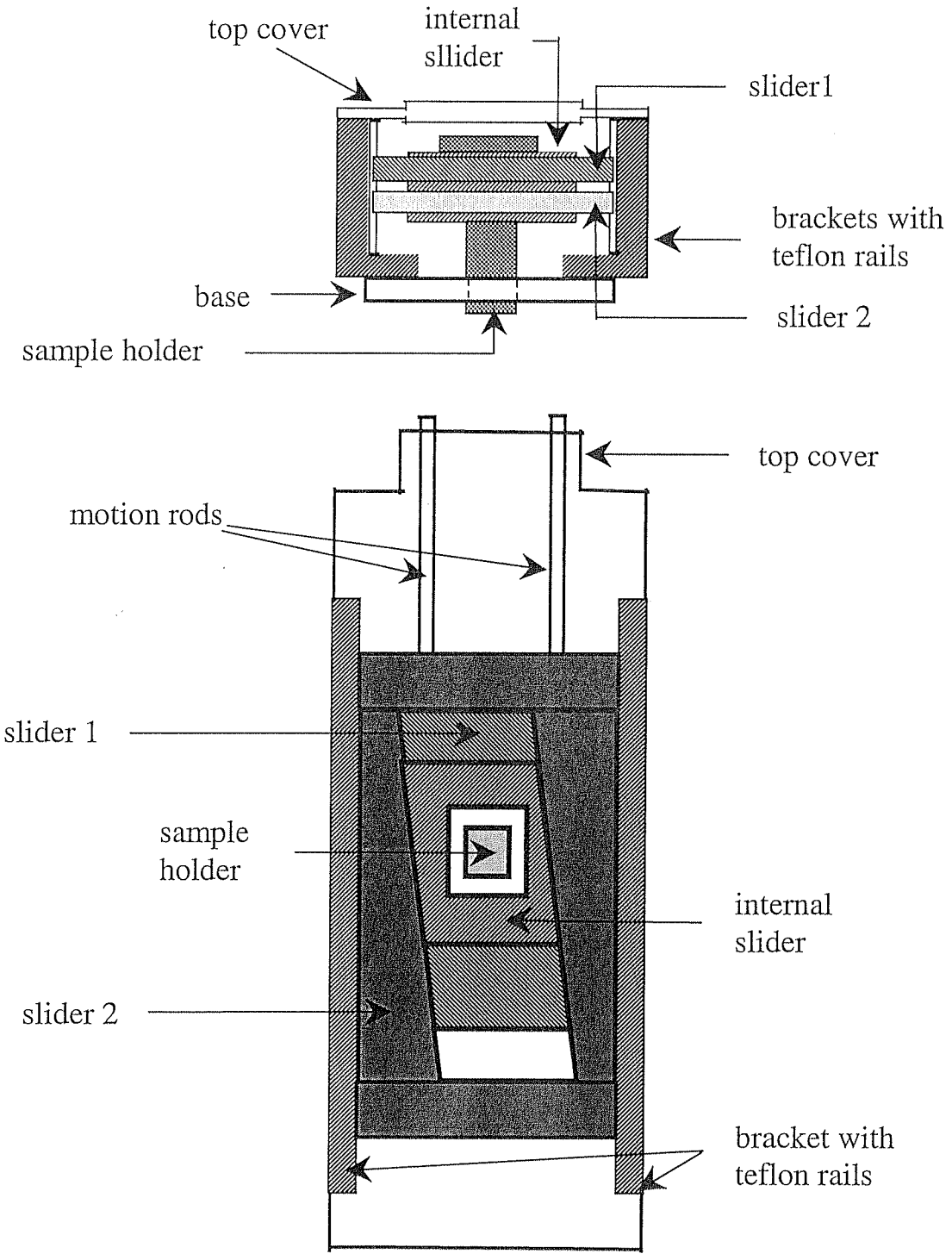

Fig. 2.5. Schematic of cold stage of 2-D scanner, (a) plan view, and (b) front view, base not shown.

moved simultaneously. Only slider 2 is moved in order to move the sample in the left or right direction. The way this works is that the sample is constrained by the horizontal groove in slider 1, which has been held fixed. The 15° edges push the sample to the right along the horizontal slot. Return springs hold the internal slider firmly against slider 2 in order to avoid hysteresis in the horizontal position of the sample.

2.3 Operation of the microscope

The microwave microscope scanner is somewhat cumbersome to work on. For example, it requires two people to lift it and place it in the dewar. To make it easier to work on the scanner, we have a holder for the microscope. While I am preparing the scanner prior to cooling it down, it lies horizontally on the mount on my lab table. During preparation, the mount allows me to rotate the scanner about its axis to easily reach various parts.

2.3.1 Leak-checking the microscope

To check the vacuum leaks in the system, I pump out the vacuum can using a turbo-pump and then connect the scanner to the leak detector. With the vacuum pumped down I can check for leaks on the 10^{-8} std cc/sec scale. Initially, I had a leak rate which was much higher than the base leak rate because of the leaks in some of the swagelok connectors used in the system. When the leaks in the swageloks were sealed, the leak rate reduced to about twice the base leak rate, probably due to outgassing from the plastics in

the scanner mechanism. This outgassing also causes the pressure in the can to rise to about 1 Torr if left overnight after being evacuated.

2.3.2 Cooling the microscope

The inner diameter for the 2-D microscope dewar is 6 inches. The dewar has a liquid nitrogen jacket around it. The nitrogen jacket is separated from the helium space by a vacuum space and a vacuum space also separates the jacket from the outside of the dewar. In order to cool the scanner, I simply place the scanner in the dewar and fill the liquid nitrogen jacket and helium space with liquid nitrogen. With exchange gas in the vacuum space, the system cools to 77 K within about an hour. I typically have to refill the dewar every day or two to keep it at 77K.

2.3.3 Automation

The scanning operation of the microscope is fairly well automated. Computer-controlled stepper motors are attached to the X-Y feedthroughs while the Z-feedthrough can be operated manually between scans. The motor system uses two skew-pole stepper motors [16], two Microstep motor drivers and a Motor Controller [17] board and power supply [18].

A visual basic program, Runtime 5, controls the motor controller board and a/d board [19]. Runtime 5 which is a slightly modified version of Randy's original program and takes images of the sample in a raster pattern. As the scan progresses the A/D board records the output voltage from a diode detector. The output is displayed on the PC

monitor. Data is only recorded on the forward part of the motion. To move the sample in the x (transverse) direction the longer feedthrough is moved. The image is taken by continuously scanning along the x-direction. In order to change the y value both the feedthroughs are moved. The scanning process is then repeated until the entire sample is imaged. A detailed discussion of the microwave portion of the microscope is included in Chapter 3.

The program automatically records the data and writes it to an output file. I view the data on a Macintosh computer using a graphics program, which is made by Fortner Inc. This program displays the data in a false-color or gray-scale image and allows for every adjustment of the color scale.

2.4 Microwave system model

We have developed a model for the microscope resonator and sample using standard microwave transmission line theory [20, 21, 22]. The model is illustrated in Figs. 2.6 and 2.7. Figure 2.6 shows a circuit diagram for the microwave source, directional coupler, and diode detector. The lumped input impedance to the resonator portion of the microscope is Z_{res}. We define the complex microwave source voltage and current to be

$$V_S = e^{i\omega t} (V_S^+ + V_S^-)$$

$$I_S = e^{i\omega t} (V_S^+ - V_S^-) / Z_C$$

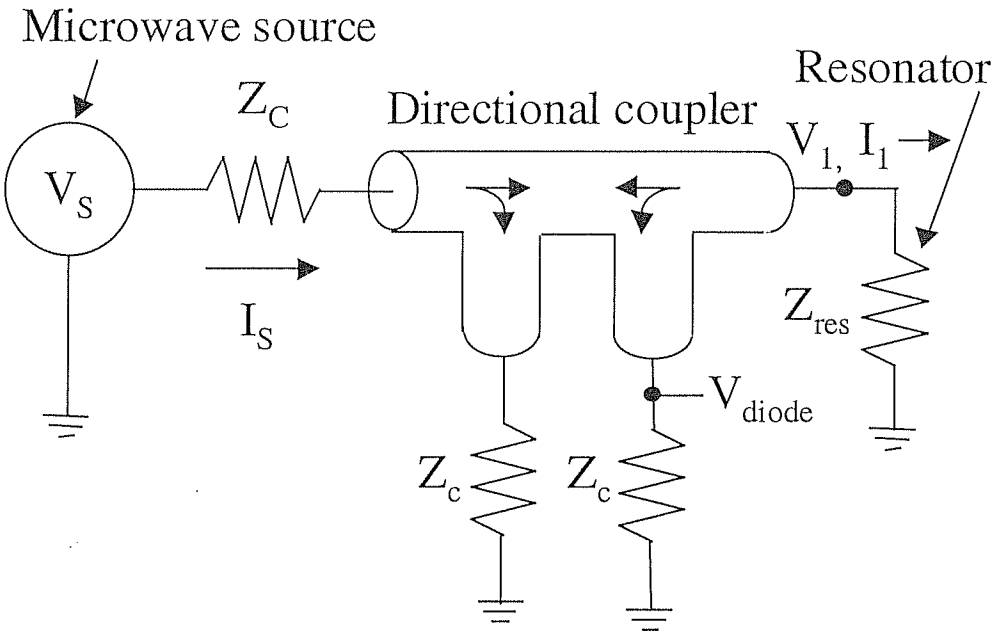

Fig. 2.6. A transmission line model for the microwave microscope

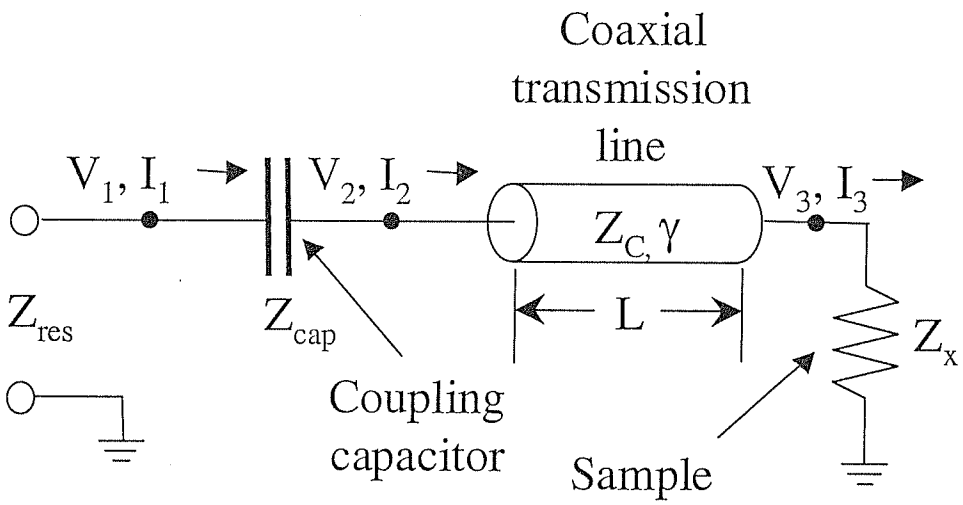

Fig. 2.7. The resonator, represented as the effective impedance Z_{res}, is modeled as shown in the above figure.

where ω is the frequency of the microwave source, and $Z_C = 50\ \Omega$ is the characteristic impedance of the coaxial cables. The quantity V_S^+ is the amplitude of the wave traveling to the right in Fig. 2.6, while V_S^- is the amplitude of the wave traveling to the left. The output voltage of the microwave source is V_S^+. We define the voltage and current at the input to the resonator to be

$$V_1 = e^{i\omega t} (V_1^+ + V_1^-) \tag{2.1}$$

$$I_1 = e^{i\omega t} (V_1^+ - V_1^-) / Z_C \tag{2.2}$$

For the directional coupler, we define the coupling voltage fraction to be $\eta \equiv 10^{\zeta/20}$, where ζ is the coupling in dB. For our directional coupler with $\zeta = -6$ dB, η is approximately 0.5. The equations for the directional coupler are

$$V_1^+ = V_S^+ (1 - \eta)$$

$$V_S^- = V_1^- (1 - \eta)$$

$$V_{diode} = -\eta V_1^- \tag{2.3}$$

Finally, we have

$$V_1 = I_1 Z_{res}. \tag{2.4}$$

Combining the above equations, eliminating V_S^-, and solving for V_{diode}, we obtain

$$V_{diode} = (Z_{res} - Z_0)\, \eta\, (1 - \eta)\, V_S^+ / (Z_{res} + Z_0) \tag{2.5}$$

The resonator portion of the circuit (Z_{res}) is shown in Fig. 2.7. The coupling capacitor impedance is

$$Z_{cap} = 1/(i\omega C_{cap}) \tag{2.6}$$

where C_{cap} is the coupling capacitance. We calculate Z_{res} as follows. We define the voltage and current at the coupling end of the resonator to be

$$V_2 = e^{i\omega t} (V'_+ + V'_-)$$

$$I_2 = e^{i\omega t} (V'_+ - V'_-) / Z_C \tag{2.7}$$

The coaxial transmission line in Fig. 2.7 is the only distributed element in the model. We take the propagation constant to be

$$\gamma = \alpha + i\beta \tag{2.8}$$

where α is the attenuation constant in nepers/m, and

$$\beta = \omega\sqrt{\epsilon} / c \tag{2.9}$$

where ϵ is the dielectric permittivity in the coaxial cable, and c is the speed of light. At the probe end of the resonator, the voltage and current are

$$V_3 = e^{i\omega t} (V'_+ e^{-\gamma L} + V'_- e^{\gamma L})$$

$$I_3 = e^{i\omega t} (V'_+ e^{-\gamma L} - V'_- e^{\gamma L}) / Z_C \tag{2.10}$$

where L is the length of the resonator. Finally, at the coupling capacitor, we have

$$I_1 = I_2$$

$$V_2 - V_1 = I_1 Z_{cap} \tag{2.11}$$

Combining the above equations, we find

$$Z_{res} = V_1 / I_1 = Z_{cap} + Z_C[(Z_x+Z_C)e^{\gamma L}+(Z_x-Z_C)e^{-\gamma L}] / [(Z_x+Z_C)e^{\gamma L}-(Z_x-Z_C)e^{-\gamma L}]$$

Thus, the diode detector voltage V_{diode} can be calculated using equations 2.5 and 2.12.

Chapter 3

Microwave near-field imaging of electric fields in a superconducting microstrip resonator

3.1 Introduction

The demonstration of low microwave loss in high-T_c superconductors at 77 K has opened up the possibility for commercial communication applications [1] which require performance beyond that achievable with existing normal-metal devices. Unfortunately, present-day thin-film high T_c microwave components have shown performance-limiting problems including nonlinearity, intermodulation, and power-dependent characteristics [2]. One important class of nonlinearities arises from vortex motion at weak links and grain boundaries [3] and is exacerbated by poor film quality or large current densities found near patterned edges [2].

Most techniques used to characterize the microwave behavior of high-T_c circuits involve global measurements which determine the response of the device as a whole [4,5]. To obtain a complete microscopic picture of non-linearity in superconducting rf devices, spatially resolved probes of microwave current distribution [6], electric and magnetic field strength [7], loss [8,9] and microstructure are needed. Conventional microwave electric field imaging techniques include using modulated perturbations [10], electro-optic techniques [11], scanning force potentiometry [12], and other local probes [13] which locally extract the signal of interest.

In this chapter, I describe how I imaged microwave electric fields in superconducting devices using a near-field scanning microwave microscope [14]. I apply this technique to a prototype device, the single-pole microstrip resonator filter, and examine both a normal metal and a superconducting version. This work establishes the foundation for my attempt to image intermodulation fields, described in Chapter 5.

3.2 Experimental Arrangement

A schematic illustration of my experimental arrangement is shown in Fig. 3.1. Microwave power is supplied by an HP 83620B signal generator with a frequency range from 0.01 to 20.00 GHz. The power is amplified by an HP 8349B amplifier to about 100 mW and fed to the microstrip resonator through an UTE Microwave, Inc., Model no. CT-4030-OT isolator and a home-made capacitive coupler. I used an open-ended coaxial probe to sense the electric fields from the microstrip (see Fig. 3.2). The probe is connected through an isolator to a matched 50 Ω diode which rectifies the rf signal to produce a dc output which is roughly proportional to power. This dc output is amplified, filtered, and recorded by a computer.

3.3 Electric Field Probe

For the images I will show in this chapter, I set up the microscope for measuring electric field. For this type of measurement, it is important to recognize that the outer conductor of the coaxial probe shields the inner conductor from lateral components of the field, allowing us to measure mainly the normal component of electric field E_z. It is also

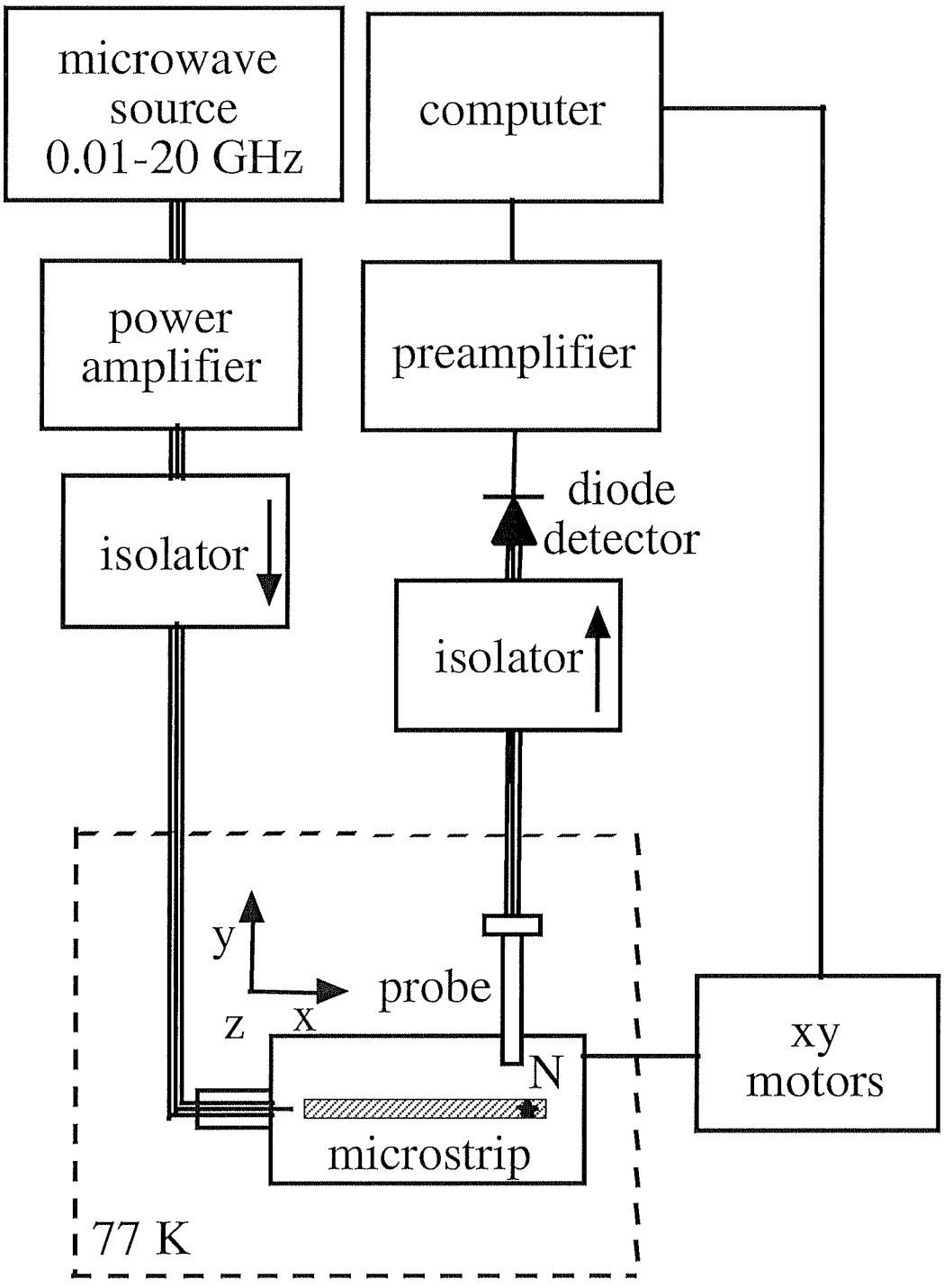

Fig 3.1. Schematic illustration of the cryogenic microwave microscope. The dashed box indicates the cryogenic section.

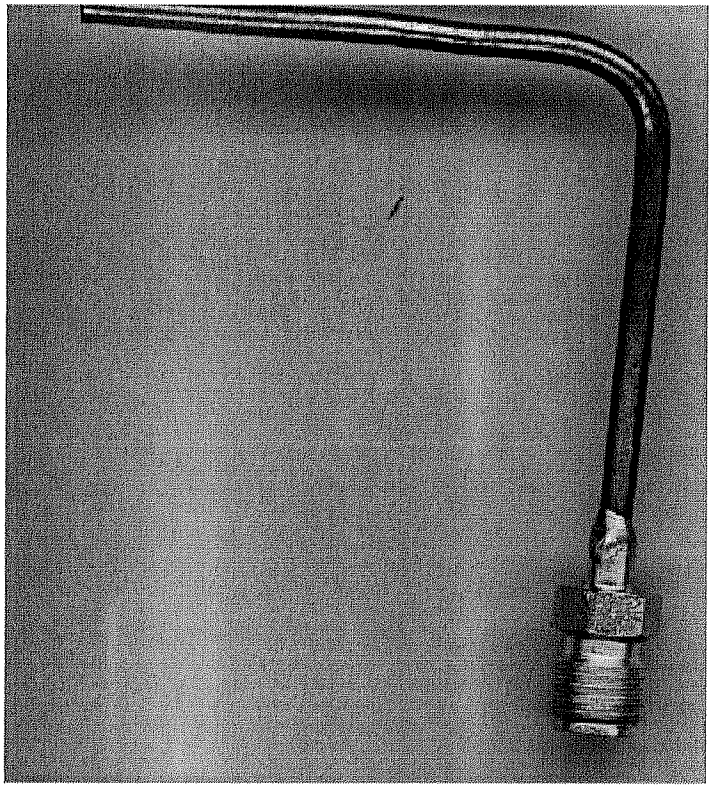

Fig. 3.2. Photograph of the coaxial probe with 500 microns inner conductor diameter.

important to recognize that this is only a rough picture of what happens. In particular, the conducting surfaces of the probe will tend to perturb the field from the sample [15]. Here I will ignore this effect.

The field E_z from a sample induces a net charge Q_I on the center conductor of the probe. According to Gauss' law, $Q_I = \epsilon_0 E_z A$ where $A \approx 0.03$ mm^2 is the area of the face of the center conductor. We can find the absolute magnitude of E_z by relating Q_I to the power P detected at the diode. The total current induced on the probe face by the electric field is $I = dQ_I/dt = i\omega\epsilon_0 E_z A$, where ω is the angular frequency. For a lossless transmission line with a characteristic impedance $Z_0 = 50\ \Omega$, the power detected by the matched diode is $P = I^2 Z_0$. Therefore, one finds $E_z = [P/(\omega^2 \epsilon_0^2 A^2 Z_0)]^{1/2}$.

The cryogenic part of the setup (see Fig. 3.1 and Fig. 3.3) is enclosed in a vacuum can which I insert into a liquid-nitrogen cooled Cryofab Model CSM 6042 Cryostat. (See Chapter 2 for a more complete description). By heating the sample mount, images can be obtained at temperatures from 77 to 300 K. After the microscope is cold, to take an image, I set the probe height, and record the diode output as the sample is moved in the x and y directions using the computer-controlled stepper motors.

3.4 Copper Microstrip Resonator

To investigate the capabilities of our system, I imaged a test copper microstrip resonator. The resonator consists of a 350-μm-thick circuit board (made from FR-4 fiberglass) which is coated on both sides with copper. One side serves as a ground plane, while the other is patterned into a microstrip which is 1.1 mm wide and L = 7.6 mm long.

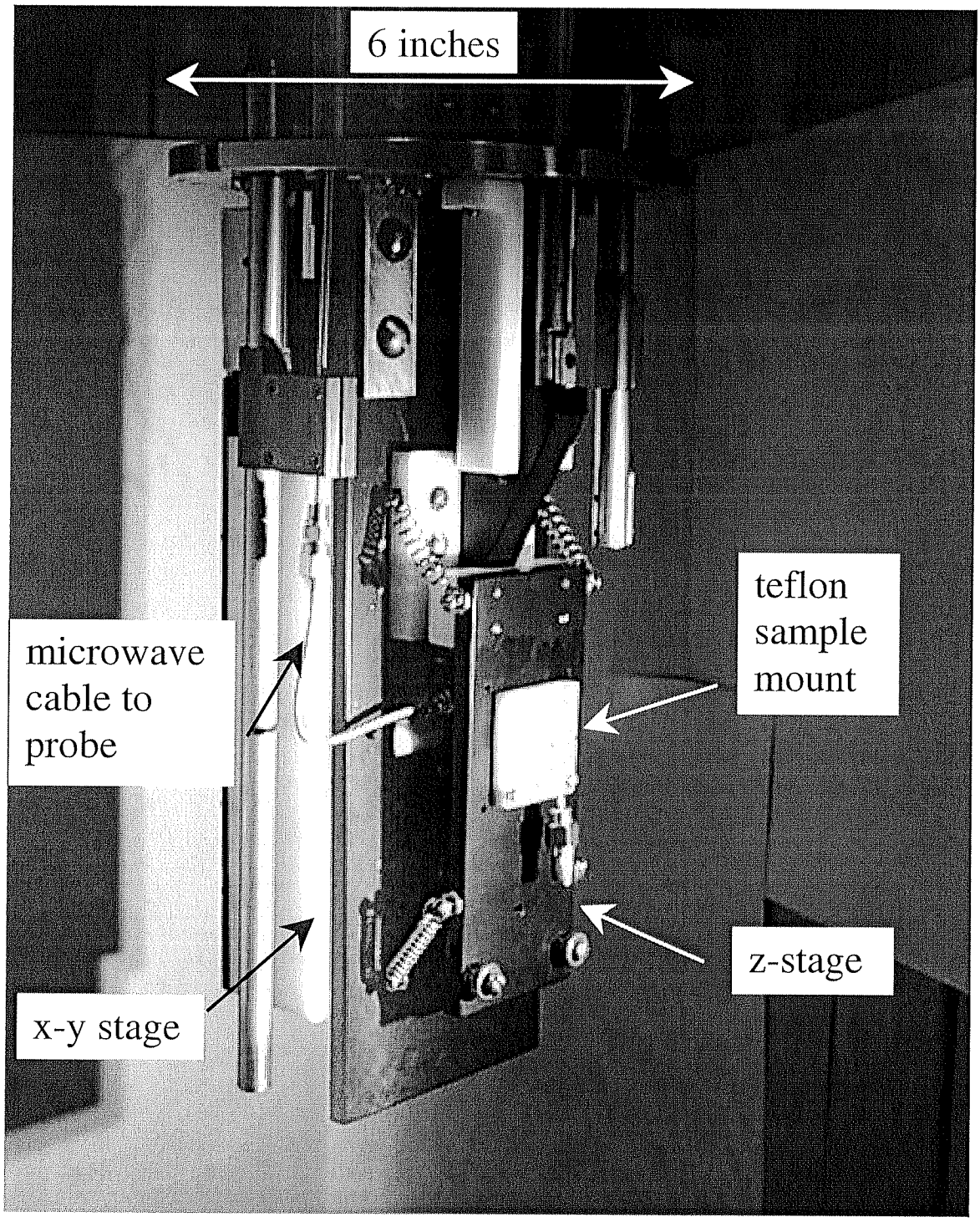

Fig.3.3. Photograph of the cryogenic part of the microwave microscope

The resonator was mounted in a Cu package and microwave signals can be capacitively coupled in and out of the resonator at one end (see Fig. 3.4).

When the resonator is excited at its resonant frequency, a standing wave pattern is created with voltage antinodes at the two ends and a voltage node in the middle. Thus we see a concentration of electric fields at the two ends. This also corresponds to current nodes at the two ends and a current antinode in the middle.

To determine the resonant frequency of the microstrip, I positioned the probe at the end of the strip at a height of 1 mm. I then applied 100mW of incident power to the capacitive coupler and recorded the diode voltage as a function of frequency. Figure 3.5 shows the rf power at the diode for temperatures of 77 and 300 K. Each curve shows a single large resonance, some small secondary resonances, and noise. The small resonances are due to reflections off components and connectors within the system. I can estimate the loaded quality factor Q of the resonator by fitting the overall frequency response with a single Lorentzian line shape. As Fig. 3.5 shows, the Q of the microstrip increases substantially as the temperature is lowered, mainly due to the improved conductivity of the copper; Q = 40 at 300 K, while Q = 92 at 77 K. From independent broadband transmission measurements at 300 K we determined the Q to be within 10% of the value given above.

At room temperature, the Cu resonator shows a peak in the detected power at about 9.64 GHz, while at 77 K the peak has shifted to 9.95 GHz. Part of the increase in the resonant frequency upon lowering the temperature can be attributed to the decreased inductance from the reduced skin depth (~ 10 MHz) and thermal contraction of the Cu microstrip (~20 MHz). From independent capacitance measurements, we found that the

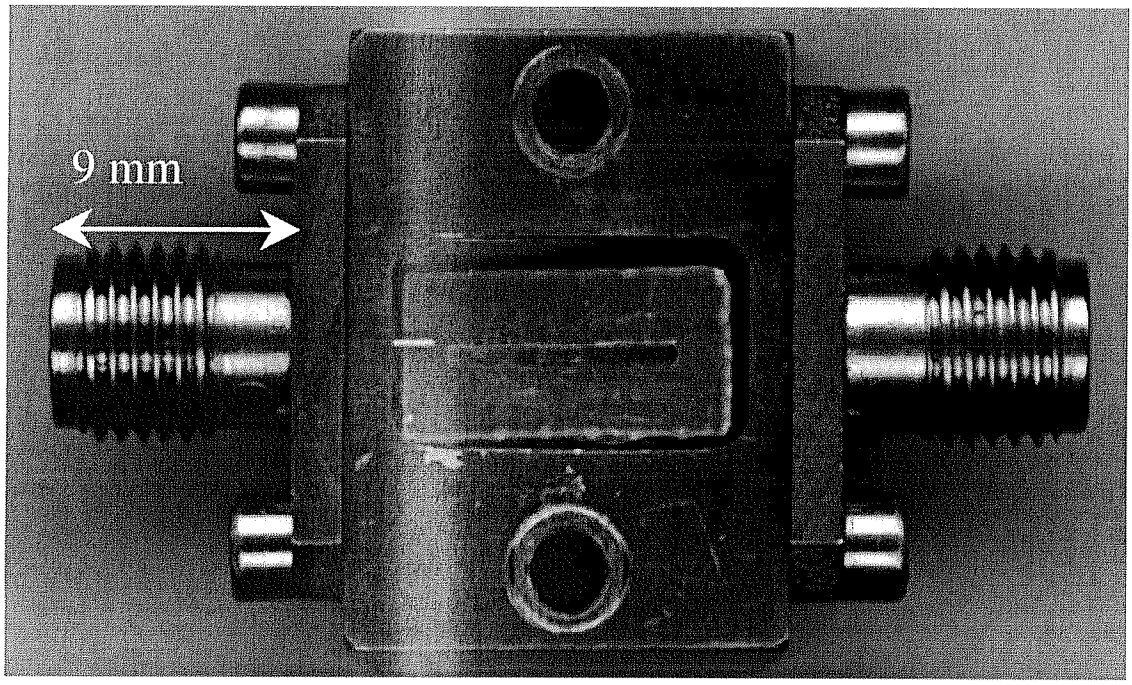

Fig.3.4. Photograph of the copper package with the copper microstrip resonator

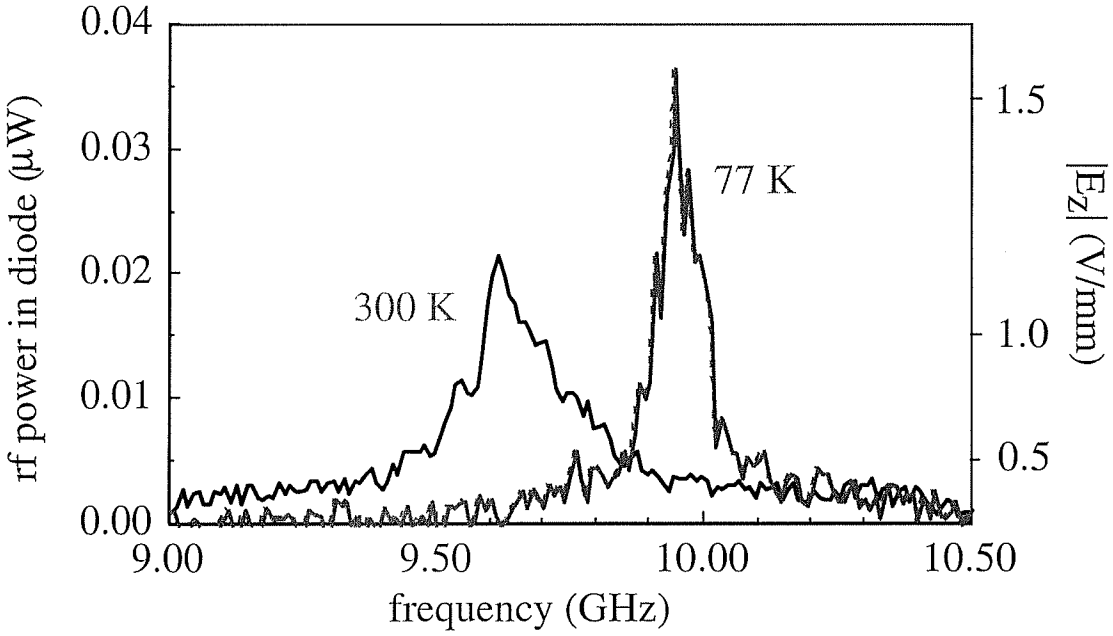

Fig. 3.5. rf power at the diode vs. frequency for copper microstrip at 77 and 300 K. The corresponding magnitude of the normal component electric field at the probe is indicated on the right axis.

310 MHz total shift is mainly due to the dielectric constant of the fiberglass substrate decreasing by 10% upon cooling. The 9.5-10 GHz resonance in Fig. 3.5 corresponds to the fundamental standing wave mode for the microstrip. This mode has voltage antinodes at the two open ends and a voltage node in the middle. This is demonstrated in Fig. 3.6, which shows a measured image of the magnitude of E_z above the Cu microstrip resonator at 77 K. During the scan, I fixed the frequency of the source at the resonant frequency (9.95 GHz) and the probe was held about 1 mm above the microstrip. The image shows a maximum signal at the two open ends of the microstrip conductor (corresponding to the voltage antinodes), and a minimum in the middle (corresponding to the voltage node), as expected.

3.5 TBCCO Microstrip Resonator

I next imaged a $Tl_2Ba_2CaCu_2O_8$ (TBCCO) microstrip resonator that was supplied by STI, Inc. The resonator has a 650-nm-thick film of TBCCO deposited on both sides of a 420-μm-thick, 4.7 mm X 9.9 mm MgO substrate. One side serves as a ground plane, while the other is patterned into a microstrip with a width of 150 μm and a length L = 7.1 mm. The resonator is mounted in a Cu package and rf power is capacitively coupled to one end (see Fig. 3.7). Figure 3.8 shows a frequency scan taken at 77 K (at point N in Fig. 3.1) with the probe at a height of about 250 μm above the microstrip. Note the much smaller frequency range, as compared to Fig. 3.5, indicating the substantially higher Q of the superconducting resonator.

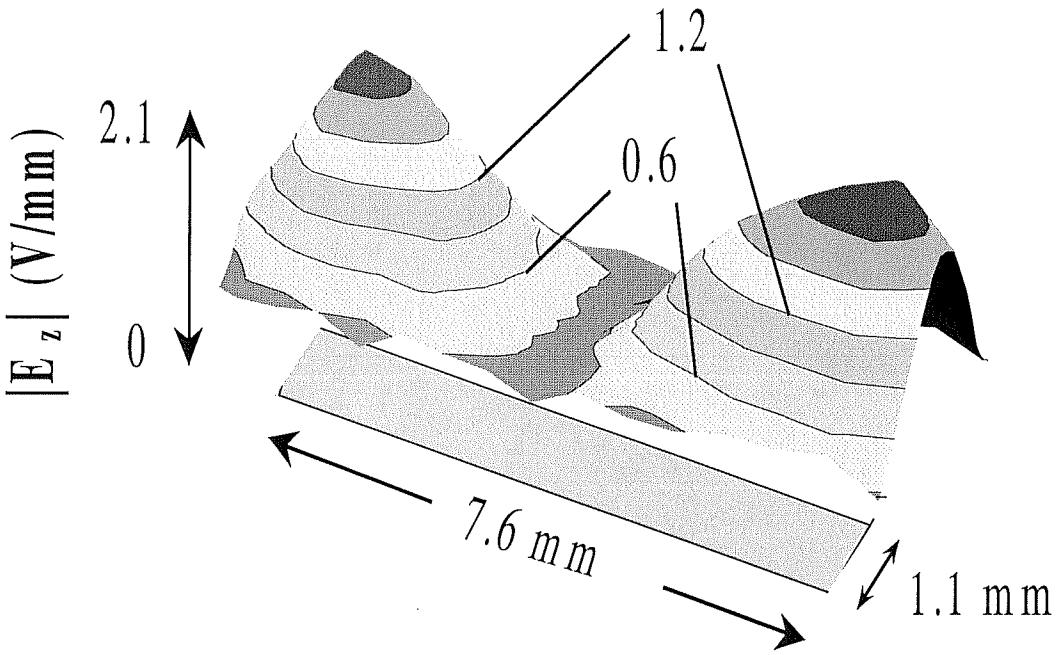

Fig 3.6. E_z above a Cu microstrip excited at its fundamental frequency (f = 8.205 GHz).

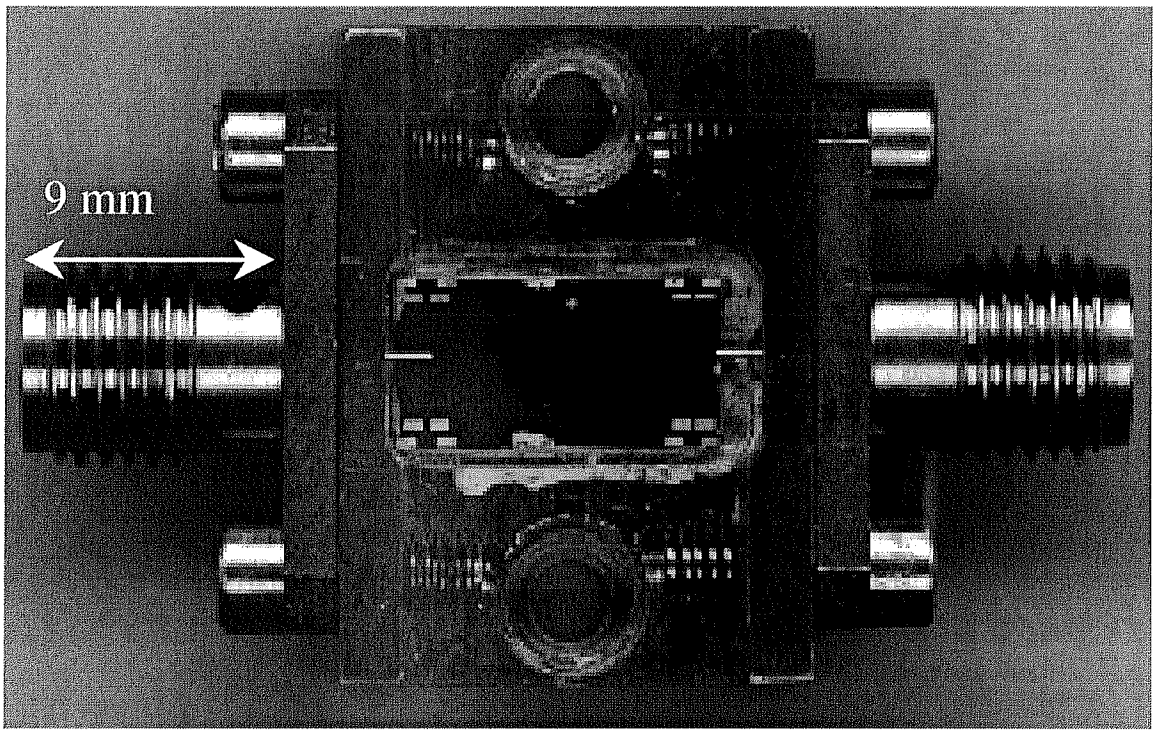

Fig. 3.7. Photograph of the Cu package with the TBCCO resonator. SMA connectors allow signal to be coupled into and out of the microstrip. Note that the output coupling pin on the right side is off the strip, while the coupler on the left side is over the strip.

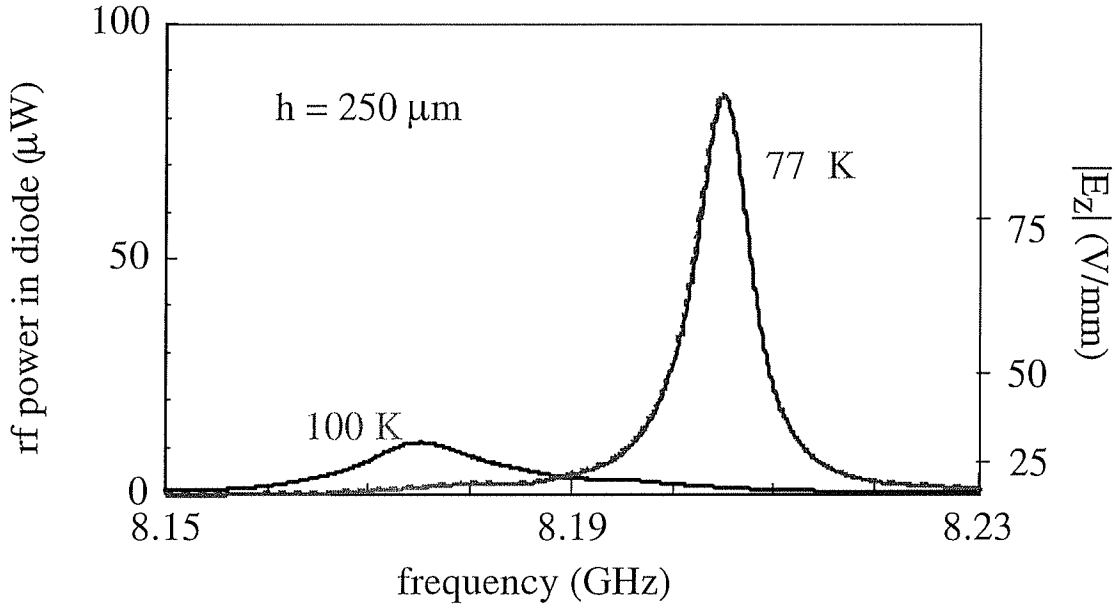

Fig. 3.8. rf power at the diode vs. frequency for TBCCO microstrip at 77 and 100 K. The corresponding magnitude of the normal component electric field at the probe is indicated on the right axes.

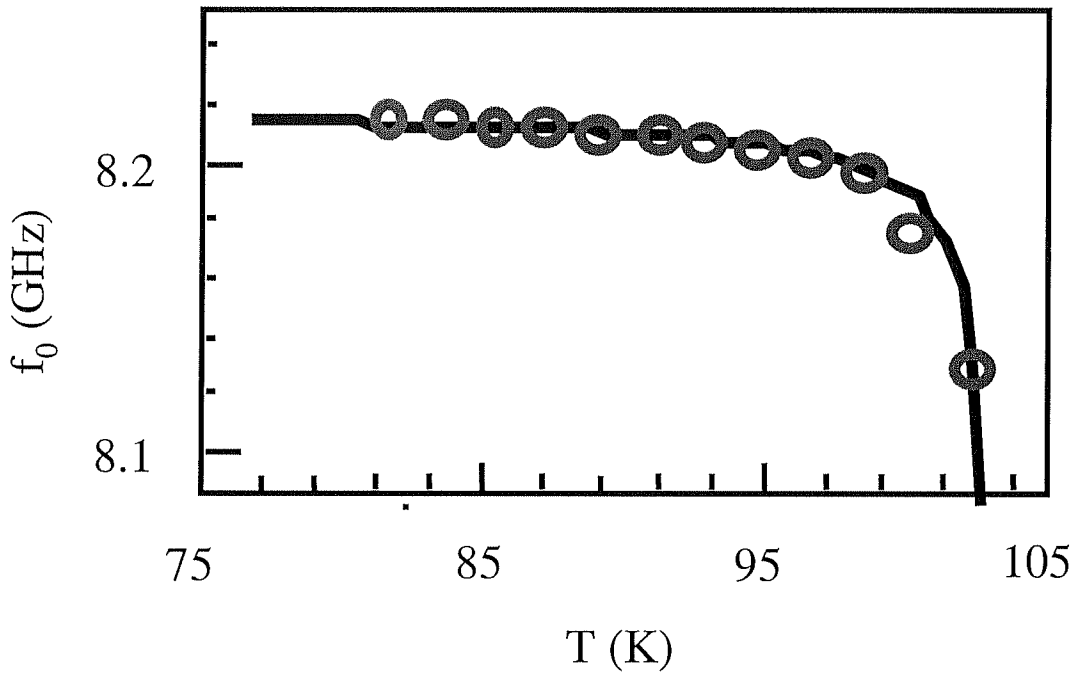

Fig. 3.9. Temperature dependence of the resonant frequency f_0 along with a fit to BCS theory (solid line).

The decrease in resonant frequency at higher temperatures is due to the increase in penetration depth λ of the superconductor. Lucia V. Mercaldo was able to fit the temperature dependence of the resonant frequency f_0 using a Bardeen-Cooper-Schrieffer (BCS) s-wave temperature dependence for $\lambda(T)$. See Fig. 3.9. The fit yields $T_c = 103.2$ K and $\lambda(0) = 0.24$ μm. The T_c is in good agreement with separate ac-susceptibility measurements (101-103 K), and $\lambda(0)$ is in good agreement with an independent determination by Willemsen et al. [$\lambda(0) = 0.26$ μm] in similar TBCCO thin films.

Analysis of Fig. 3.8 shows that the loaded Q goes from about 1200 at 77 K to about 480 at 100 K, with a temperature dependence very similar to the one observed for f_0. See Fig. 3.8. The measured Q at 77 K allows us to put an upper bound on the surface resistance of TBCCO: $R_s \leq 11.3$ mΩ at 8.205 GHz. However, the Q is about a factor of 2 lower than the value measured using a network analyzer in the absence of the probe, suggesting that coupling to the probe contributes significant loss.

Figure 3.10 shows $|E_z|$ above the TBCCO microstrip resonator, measured at 77 K. The frequency of the source is fixed at the resonant frequency (8.205 GHz) and the probe is 180 μm above the microstrip. As with the Cu resonator, we observe a maximum electric field at the two open ends, as expected for the fundamental mode. However, the field strength is quite different at the two antinodes. This is probably due to the presence of the input capacitive coupling pin on the resonator's left hand side, which perturbs the strip's simple geometry and also affects the perturbation of the resonance frequency by the probe. In addition, I note that E_z is much larger than in Fig 3.10 (up to 100 V/mm) than in Fig. 3.6 (up to 2.1 V/mm), due to the higher Q of the TBCCO microstrip and the smaller probe-sample separation.

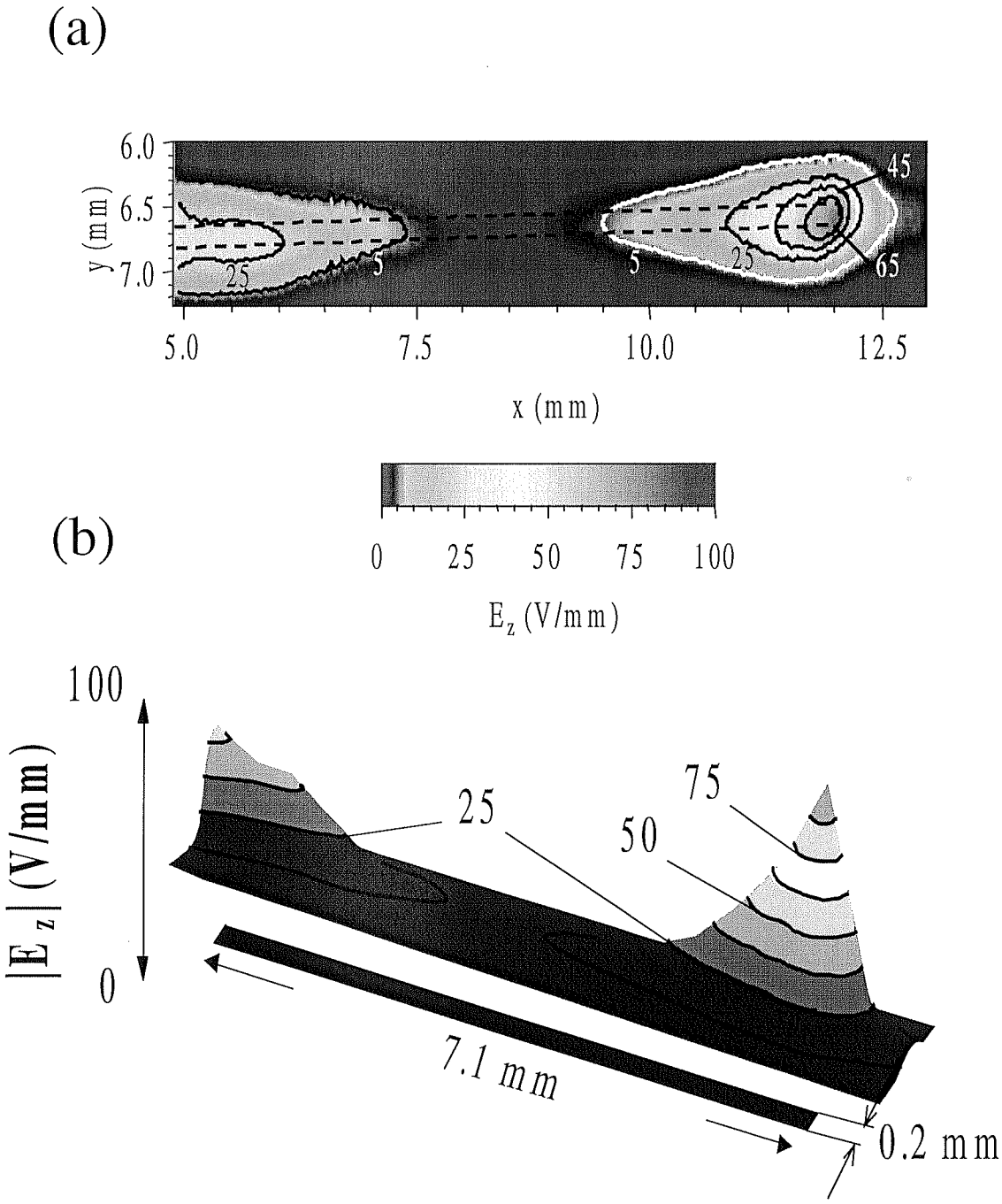

Fig 3.10 E_z above a TBCCO microstrip excited at its fundamental frequency (f = 8.205 GHz). (a) gray scale image, (b) surface plot.

As a check on the system, I also tried exciting the strip at the next harmonic. Figure 3.11 shows an electric field image obtained at 16.2 GHz, where there is also a peak in the response of the microstrip. For this image the probe was held 250 μm above the microstrip. We see a complete standing wave pattern with antinodes at the two open ends and the middle of the microstrip, as expected for the second harmonic resonance. The TBCCO strip appears to be fairly well resolved, consistent with a spatial resolution on the order of the 200 μm probe size and the probe-sample separation.

In conclusion, I have demonstrated a simple broadband microwave imaging system which allows us to measure the normal component of electric field near an operating high frequency device at cryogenic temperatures. The system has achieved about 200 μm spatial resolution using only simple microwave instrumentation combined with a cryogenic scanner, establishing the basis for a microwave examination of superconducting microwave devices. As I will discuss in the following chapter, the images do have some peculiarities, due to perturbations of the sample by the probe.

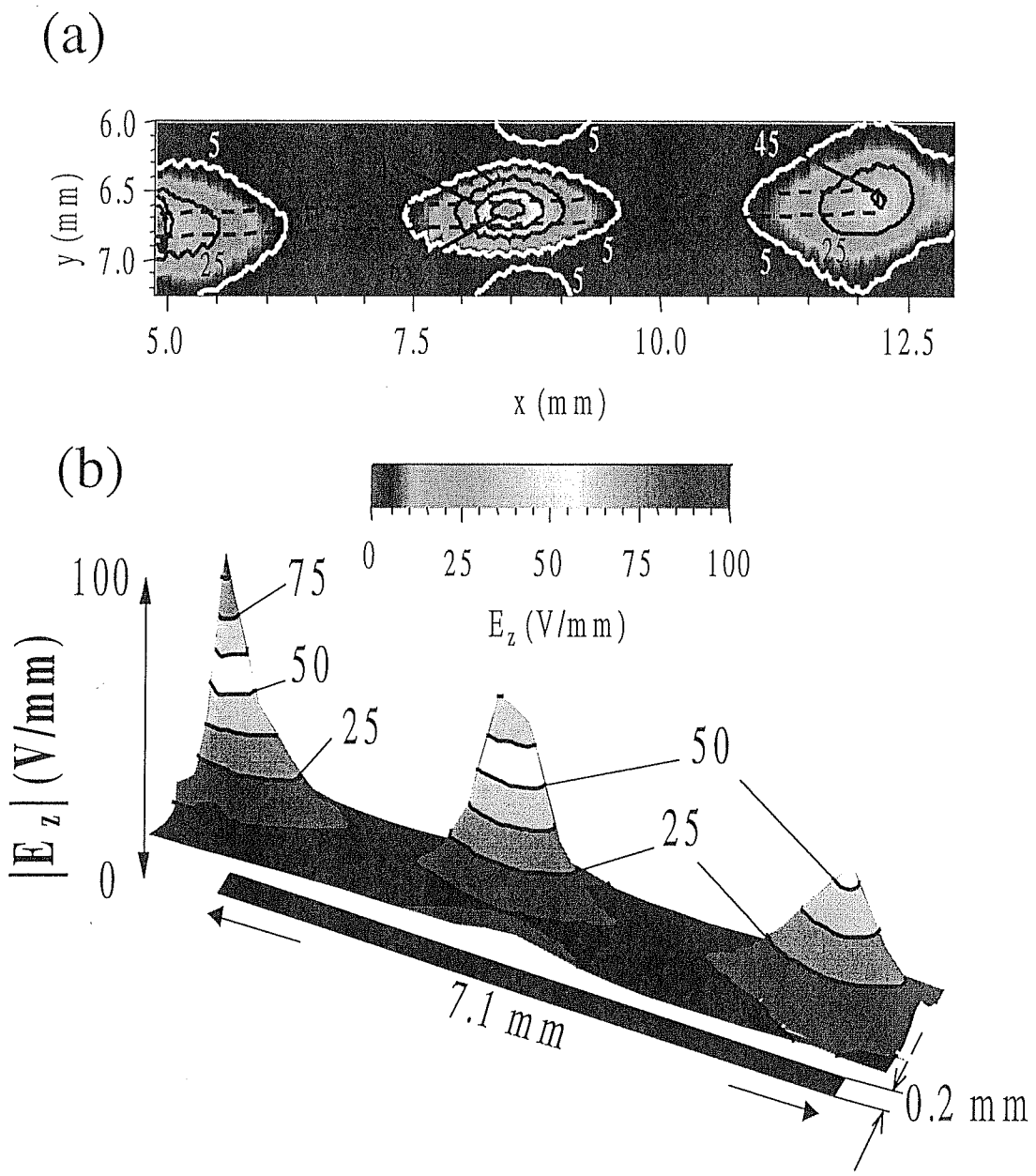

Fig 3.11 E_z above a TBCCO microstrip excited at its second harmonic frequency (f = 16.2 GHz). (a) gray scale plot, (b) surface plot. The contour lines are labeled with field strength in V/mm. In all cases, power is fed into the microstrip on the left hand side and the temperature is 77 K.

Chapter 4

Perturbation effects in the imaging of electric fields from resonant superconducting devices

4.1 Introduction

In general, I have found that extracting quantitative local information from microwave images of resonant structures is difficult to achieve. One of the biggest problems is that the probe perturbs the system. In the previous chapter, I showed some of my work on imaging high-Q superconducting resonators. While it was possible to obtain images of the fundamental mode and next harmonic, in fact the images themselves show some anomalies. As I will discuss in this chapter, the anomalies appear to be mainly due to the perturbation caused by the probe itself. Given the relatively high Q of the system, it is not too surprising that perturbations are obvious: What is less clear is what can be done about them !

4.2 Experimental Setup

Figure 4.1 shows my standard experimental arrangement for imaging electric fields at a fixed frequency. As I described in Chapter 3, an HP 83620B signal generator, supplies the microwave power. This power is amplified by an HP 8349B amplifier to about 100 mW and fed to the superconducting microstrip filter through an isolator and a

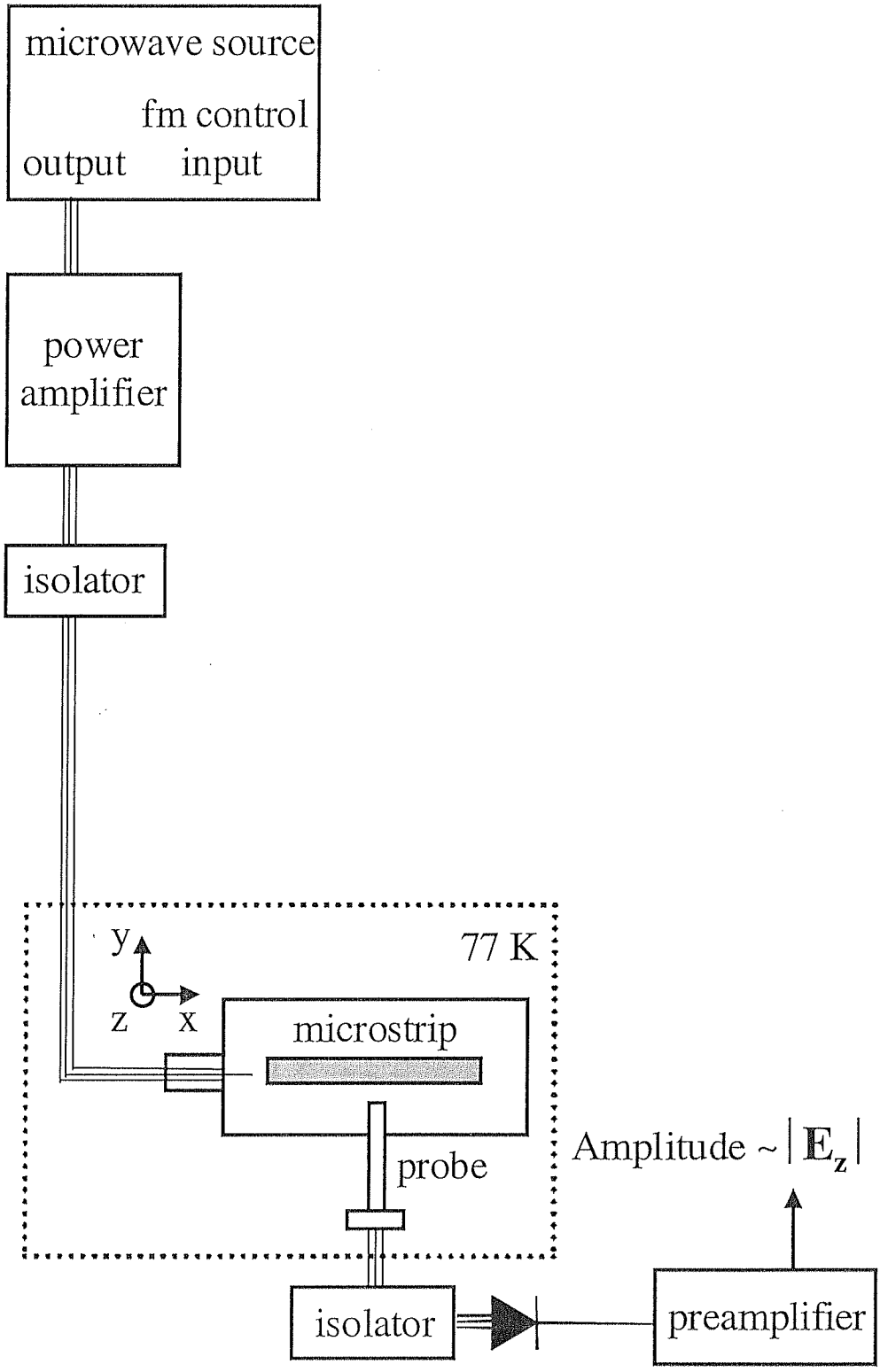

Fig. 4.1. Schematic of cryogenic microwave microscope. The dotted box indicates the cryogenic section.

pin which capacitively couples to the end of the microstrip. The electric field above the microstrip is picked up by an open-ended coaxial probe. For the images in this chapter, I used a probe with an inner conductor diameter of 200 μm and an outer conductor diameter of 810 μm.

I measure the electric field distribution from the sample coupled to the probe. The resulting microwave power passes through an isolator to a diode detector, which produces a dc-output proportional to the incident rf-power. The diode output is amplified, filtered, and recorded by a computer, which also controls the sample position using a two-axis cryogenic translation stage. It is important to note that in this configuration, the electric field image is obtained at a fixed frequency.

4.3 Sample Description

The sample I imaged was the same $Tl_2Ba_2CaCu_2O_8$ (TBCCO) superconducting single-pole microstrip resonator that I described in Chapter 3. A photograph of the package and the sample is shown in Fig. 4.2. The TBCCO strip is about 7.1 mm long and 150 μm wide. The capacitive coupling pins and SMA connectors can be seen on both sides. During my measurements presented below, I removed the pin shown on the right hand side, allowing me to image beyond the end of the microstrip. With this arrangement, the resonator is electrically open on both sides, implying that the voltage, and therefore the electric field, should be maximal at the ends of the microstrip for all resonant modes.

Before imaging the microstrip, I measured S_{21} using the probe. The probe was situated about 250 μm above the open end of the microstrip, opposite to the power pin. The resulting frequency sweep, measured at 77 K, is plotted in Fig. 4.3. As I showed in

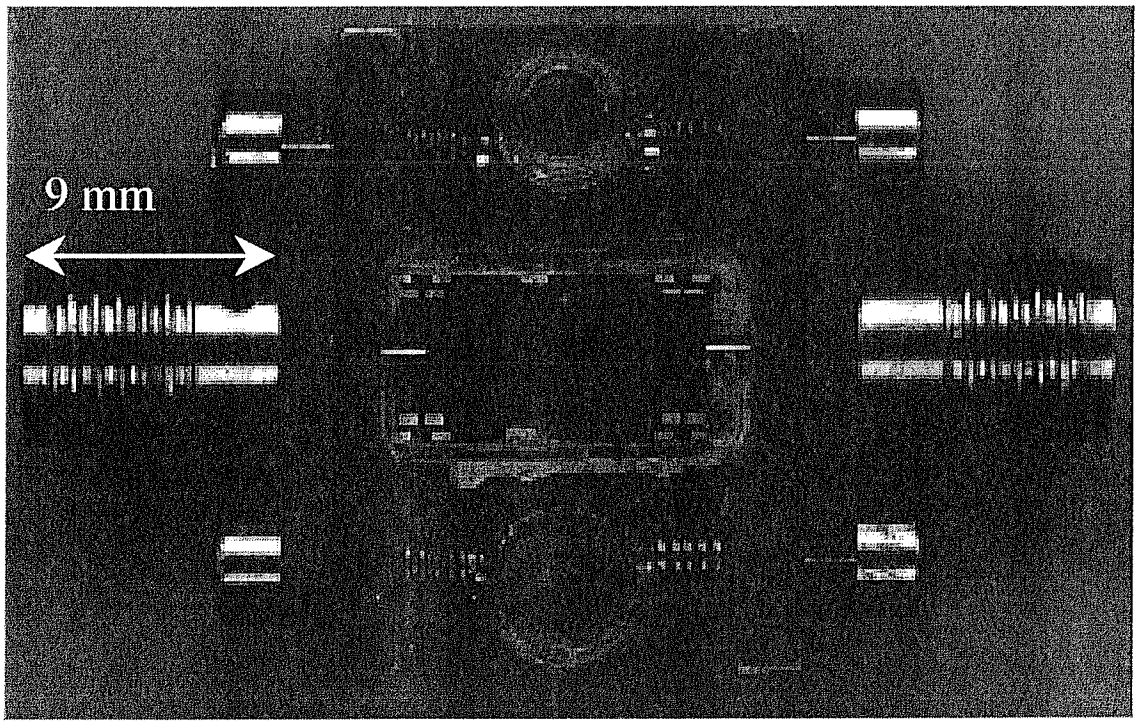

Fig. 4.2. Photograph of the Cu package with the TBCCO resonator mounted inside.

the previous chapter, the resonant frequency is $f_0 \simeq 8.205$ GHz, and the loaded quality factor is $Q \simeq 1200$. Also, the absolute value of the electric field $|E_z|$ (right axis) has been obtained by converting the power measured at the calibrated diode detector using $E_z = [P/\omega^2\varepsilon_0^2A^2Z_0]^{1/2}$ (see Chapter 2), where $Z_0 = 50\ \Omega$ and $A \approx 0.03$ mm^2

4.4 Images at different heights

In order to better understand the electric fields generated by the microstrip, I imaged the TBCCO resonator at several different heights. The idea is that such an investigation can provide useful information about the perturbation of the resonator by the probe, because the coupling to the probe will vary with the height. Thus when the probe is scanned high above the sample, the perturbation should be quite small compared to when the probe is scanned close to the sample.

Figure 4.4 (a)-(c) show images taken at heights of 1000, 500 and 180 μm, all obtained at a fixed frequency of 8.205 GHz. As expected for the fundamental mode, all the images show two antinodes, at the end of the microstrip. Also as expected, the maximum magnitude of the electric field increases rapidly (from about 2.6 V/mm to 90 V/mm) as the probe-sample distance decreases and is largest at the open ends of the sample. In fact, by 1000 μm, the signal has decreased so much that the system noise is readily evident. From the scatter in the electric field image shown in Fig. 4.4 (a), I can estimate that the noise in the system is about 0.3 V/mm at 10 GHz for an averaging time of 30 ms/pixel.

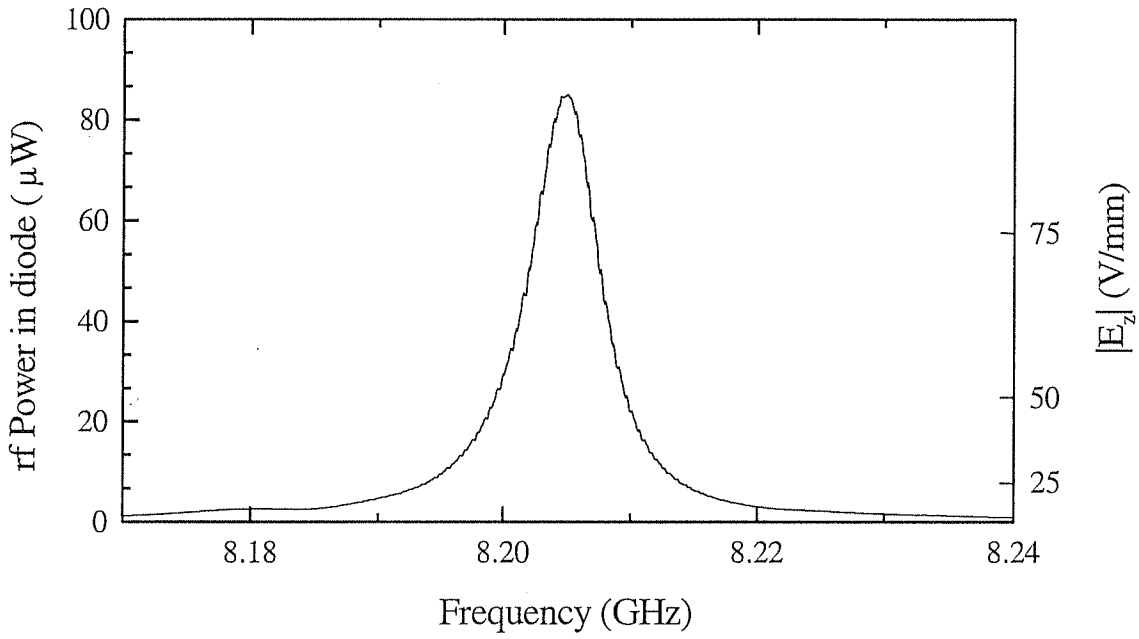

Fig. 4.3. Frequency response of the TBCCO microstrip at a temperature of 77 K, as measured with the 200 μm microscope probe at 250 μm above the sample.

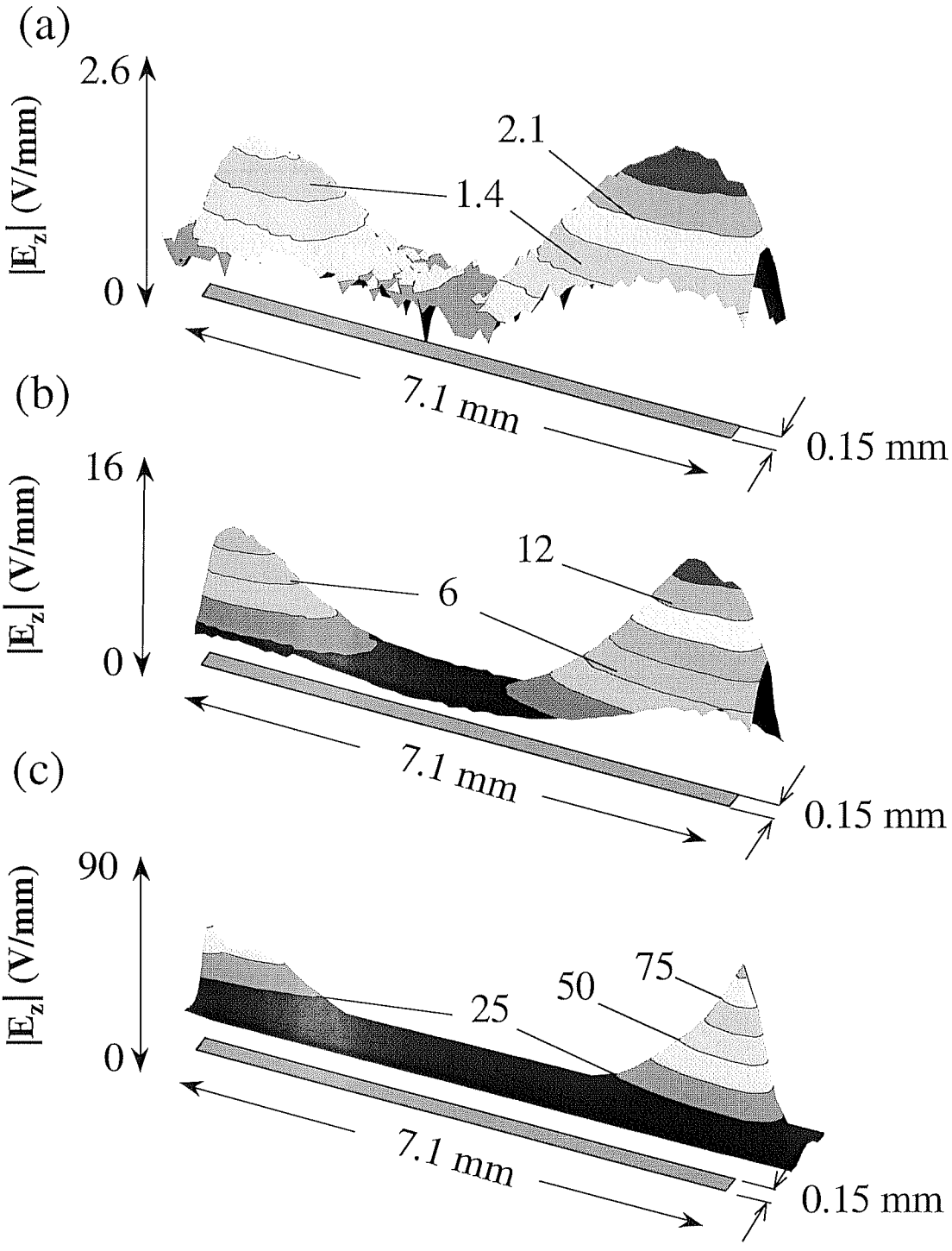

Fig 4.4. Absolute value of E_z above an operating $Tl_2Ba_2CaCu_2O_8$ microstrip resonator, measured at probe heights of (a) 180 μm, (b) 500 μm, (c) 1000 μm. The contour lines are labeled in V/mm, and the microwave power is supplied on the left hand side.

Besides the quantitative differences evident in Figs. 4.4 (a)-(c), there are also some striking qualitative differences. First, none of the images shows the $\cos^2(x\pi/L)$ dependence one might naively have expected for a microstrip. The first thing to realize is that we are sensitive to the electric field, rather than voltage. While the voltage is expected to have a $\cos^2(\pi x/L)$ dependence, the electric field tends to be concentrated at the ends of the narrow microstrip. This is most clearly seen in the image taken at the closest separation. For the other images, the height is considerably larger than the microstrip width and the inner conductor diameter. In this limit, the height determines the spatial resolution and therefore all features are broadened. Intuitively one might expect that, as long as the height is larger than the inner conductor diameter, the electric field image will sharpen as the probe approaches the device. However, the peaks observed in the 180 μm image appear to be even sharper than the 200 μm spatial resolution expected for our probe. As we will see in the next section, this puzzling discrepancy is due to the perturbation of the resonant frequency by the probe.

The second noteworthy qualitative feature in Figs. 4.4 (a)-(c) is the curvature of the peaks. At 1000 μm and 500 μm the peaks show a simple convex shape, as one would expect. However, the peaks show a concave curvature at the smallest heights, indicating a very rapid decrease in amplitude away from the antinode. The fact that this effect is only evident at close separation, strongly suggests that the change in curvature is due to perturbation of the system by the probe. I would like to point out that these features are easily overlooked, and in fact can be hidden by using a 2D plot (See Fig. 4.5).

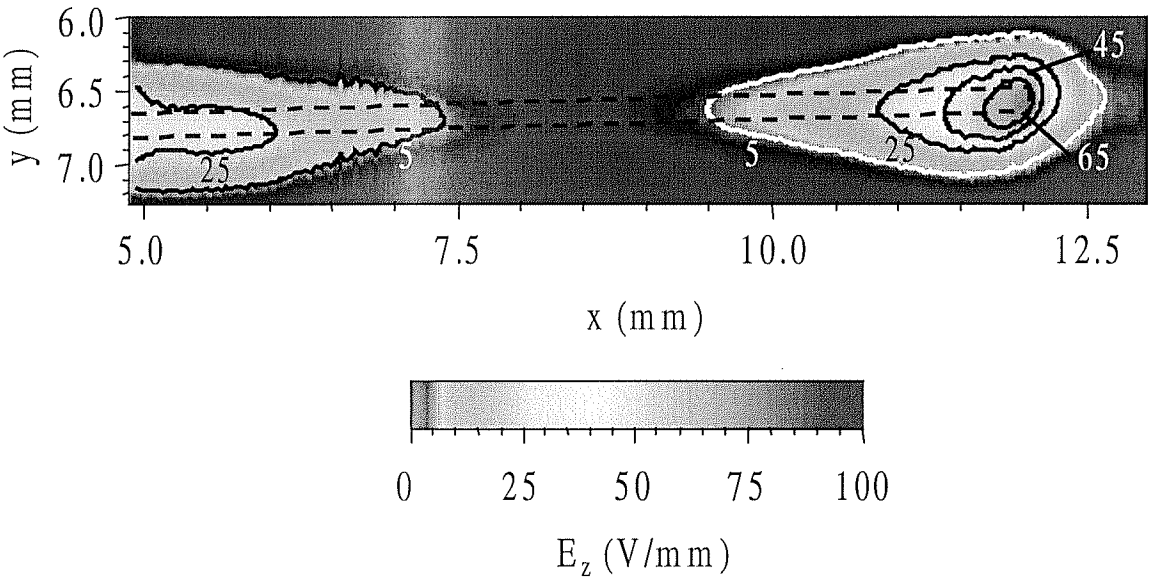

Fig 4.5. Absolute value of E_z above an operating $Tl_2Ba_2CaCu_2O_8$ microstrip resonator, measured at probe heights of 180 μm. The contour lines are labeled in V/mm, and the microwave power is supplied on the left hand side.

4.5 Electric Field Image in the Frequency-Following Mode.

While the qualitative changes in the electric field image with height were highly suggestive evidence for probe-perturbations effects, they were far from conclusive. To determine the extent to which perturbations of the resonant frequency affects our images, I tried imaging the electric field from the microstrip with the microscope operating in the frequency-following mode [1] (see Fig. 4.6).

This technique was originally developed by David Steinhauer [1] and I found it to be very useful for looking at high-Q devices. Figure 4.6 shows the configuration of the system in the frequency-following mode. First, I modulate the frequency of the microwave source and monitor the signal that is reflected from the input port of the device. The reflected power is extracted using a directional coupler, amplified, and fed to two lock-in amplifiers. The lock-ins measure the resonant frequency f_0 and the quality factor Q. To do this the frequency of the microwave source is modulated at a rate f_{FM} = 3 kHz. One of the lock-in amplifiers is referenced at f_{FM}, yielding an output signal that is proportional to the shift of the resonant frequency of the device Δf_0. This signal is used to keep the source frequency locked to the resonant frequency of the device. The second lock-in amplifier is referenced at $2f_{FM}$, yielding a signal that is proportional to the curvature of the resonance around its peak. The curvature is roughly related to the quality factor Q. Second, as all this is going on I also measure the amplitude of the electric field at the probe and record this as it scans.

When properly operated, the microscope finds the resonant frequency at each point and measures the amplitude. The main difference from the fixed frequency mode is that as the probe moves around and perturbs the resonant frequency, the source will tune

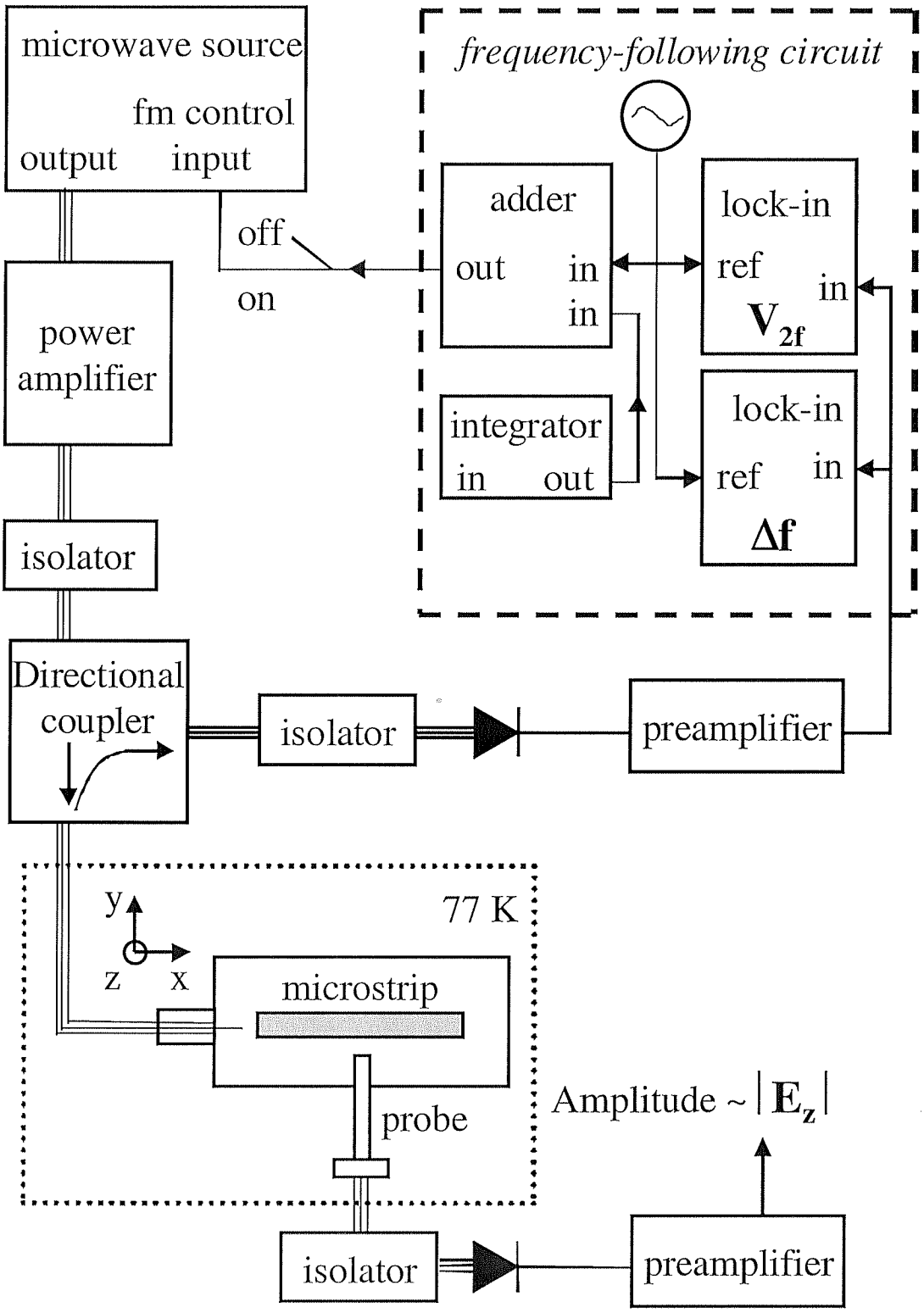

Fig. 4.6. Schematic of cryogenic microwave microscope. The dotted box indicates the cryogenic section and the dashed box indicates the frequency following section.

itself automatically to the resonance. Since it was not possible to image the left antinode entirely, due to the presence of the pin, I focused on the antinode on the right hand side. Figure 4.7 (a) shows the result using frequency-following at a height of 230 μm, while Fig. 4.7 (b) shows the corresponding image measured at fixed frequency. In comparison to the fixed-frequency image (Fig. 4.7 (b)), $|E_z|$ taken with frequency following (Fig. 4.7(a)) shows a markedly different curvature. Essentially we have recovered the expected convex peak shape. Another way to say this is that the curvature found using frequency following is very similar to that found at large (1000 μm) separations in the fixed frequency mode. (see Fig. 4.4).

The above results can naturally be explained qualitatively by realizing that the probe creates an electric field perturbation at the ends of the microstrip (where the electric field is largest). This capacitive loading tends to lower the resonant frequency of the device [2]. Since Fig. 4.7 (b) was acquired at a fixed frequency that was determined at the center of the antinode, at that particular position the system is on resonance. When the probe is moved to a different position, where the field is lower, the perturbation is reduced, shifting the resonance frequency up. As a result, for fixed frequency the measured $|E_z|$ drops considerably faster than the actual field values if there were no probe perturbation. This effect will be much more evident at closer separations at the ends of the probe, where the electric field perturbation and resulting frequency shifts are largest.

4.6 Resonant Frequency Mapping

Although the above explanation is plausible, to be completely convincing, one needs to examine the actual perturbations of the resonance frequency. To do this, I also

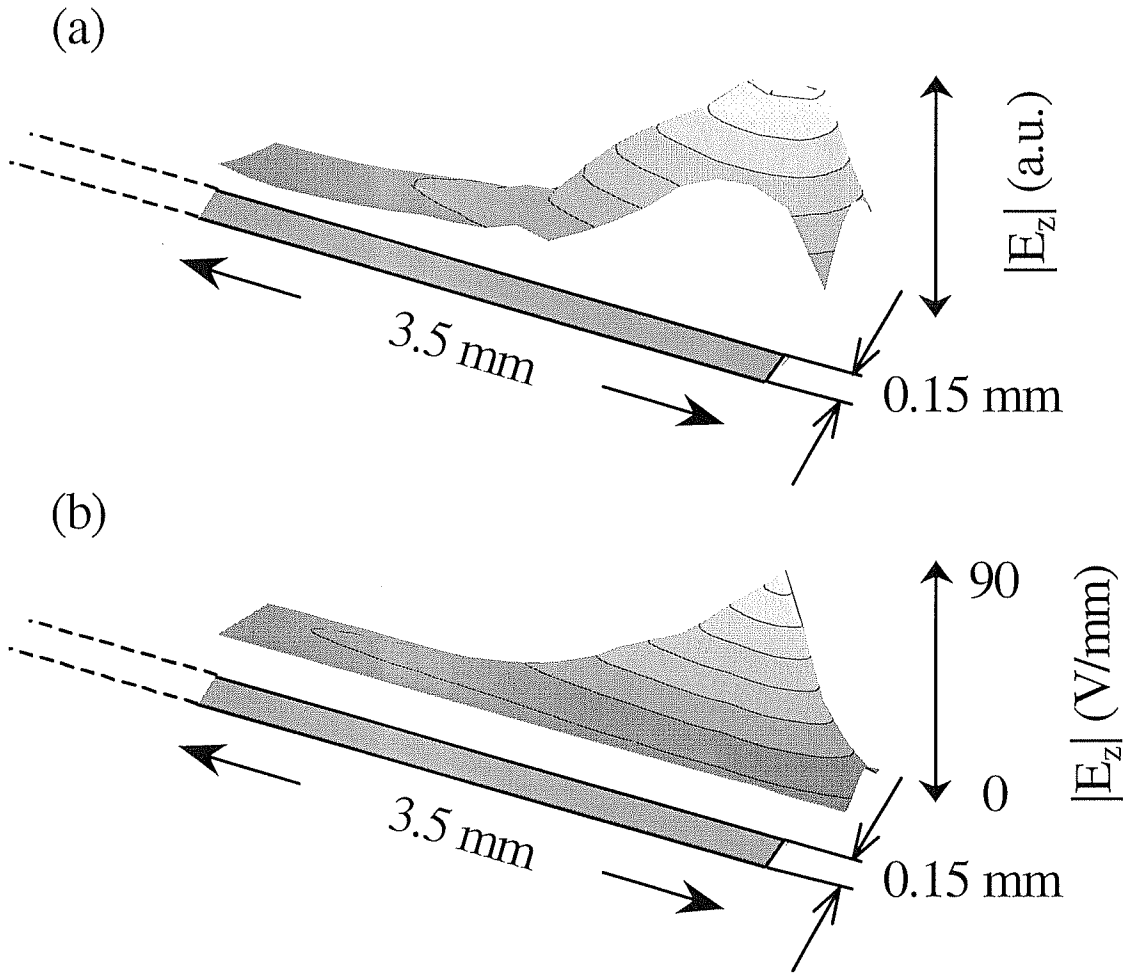

Fig. 4.7. Comparison of electric field amplitude measured (a) in the frequency-following mode and (b) at a fixed frequency, 8.205 GHz. I measured (a) at h = 230 μm and (b) at 180 μm above the TBCCO resonator.

monitored the resonant frequency while scanning the probe across the sample. This is available as the output of one of the lockins in the frequency following circuit (see Fig. 4.6). We can use this information to check whether the differences in Fig. 4.7 (a) and (b) are mainly due to the shifting of the high-Q resonance or some other effect.

Figure 4.8 shows a plot of the frequency vs. the probe position for the whole stripline. As expected, the resonant frequency shifts considerably, being minimal at the electric field antinodes (8.18 GHz).

I can also compare the frequencies in Fig. 4.8 with the value measured without the probe present. In the unperturbed case I found a resonant frequency around 8.225 GHz. This means that in the middle of the strip the resonant frequency is, in fact, **higher** than the unperturbed value. This effect is presumably due to the fact that there is an antinode in the magnetic field in the center of the microstrip. Placing the probe over the center of the strip will tend to screen the magnetic field, lowering the microstrip's inductance and increasing the resonant frequency [2]. The fact that the frequency is highest above (y = 0.6 mm) and below (y = 0.75 mm) the microstrip suggest that the probe's jacket may be the main source of the screening.

4.7 Conclusions

In this chapter, I described qualitative evidence for perturbation effects in images of a high-Q superconducting resonator. I also described the use of a frequency-following circuit that allows the microscope to track perturbations of the resonant frequency, mitigating some of the probe-perturbation effects.

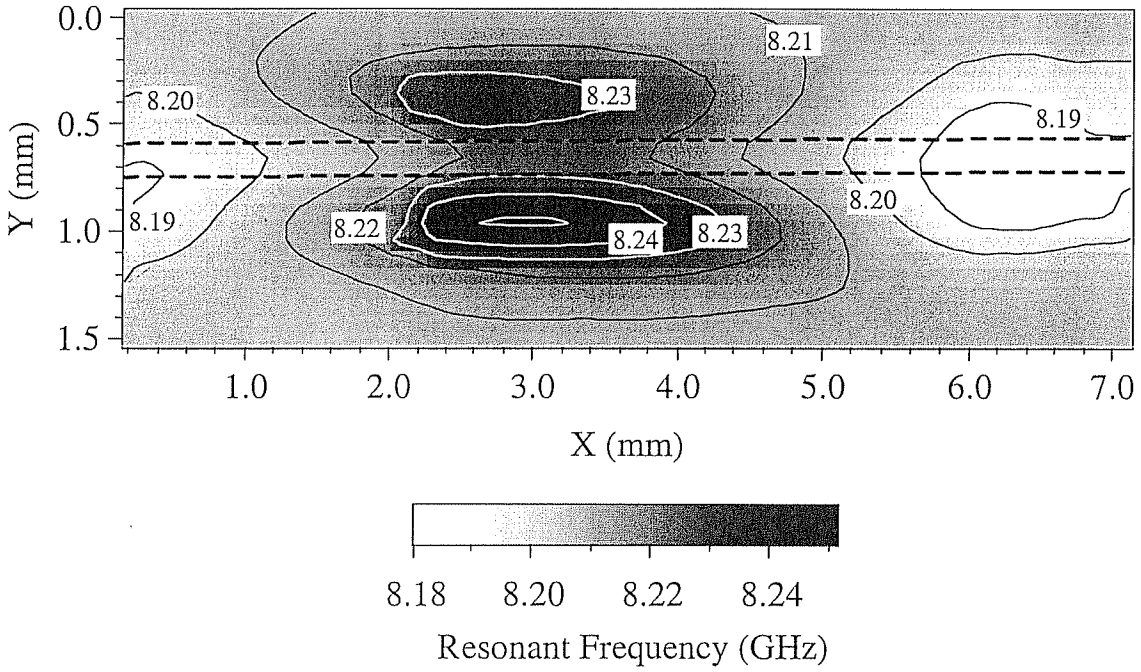

Fig. 4.8. Resonant frequency measured as a function of probe position above the TBCCO resonator. The dashed lines indicated the edges of the microstrip and the contour lines are labeled in GHz.

Chapter 5

Imaging of microwave intermodulation fields in a superconducting microstrip resonator

5.1 Introduction

The use of high temperature superconductors in passive and active microwave applications is presently restricted to low power operating conditions. The problem is that as power increases, dissipation increases in the superconductors. This non-linear response to applied power produces serious side-effects in some applications. In particular, in communications applications non-linearities produce mixing and intermodulation.

A very promising application for high temperature superconductors (HTS) is in filters for cellular telephone base stations. These stations must communicate with low-power transmitters, personal cell phones, within their assigned cells. There are competing concerns which govern the size of a cell. Fewer base stations are clearly more economical, but signal strengths at the base station are smaller, and the probability of dropped calls increases. If the base station receiver system can be made more sensitive, or if the front-end filtering can have a reduced noise figure, the cell area can be made larger. Another concern is the abundance of interfering signals present in the cellular communication frequency bands (800-900 MHz, and just below 2 GHz). Interfering signals can come from neighboring users in the spectrum, or from multiple users in a given frequency band.

Filters made from HTS materials can help to solve both of the above problems.

Band pass filters are made by patterning coupled multipole resonators in thin films of HTS on high dielectric constant substrates. Compared to conventional normal metal filters, the structures are quite compact and have very little insertion loss when operated at temperatures less than about two-thirds of the superconducting transition temperature, T_c. Because the filter must be cooled, one has the opportunity to add other cryogenic devices to the front end, such as a cooled semiconductor low-noise amplifier. The combination of reduced insertion loss and lower noise figure in the amplifier make superconducting front-end filters very attractive for use in cellular networks.

As mentioned above, an attractive aspect of HTS front-end filters is their reduced size compared to conventional copper filters. Multiple pole filters can be made from HTS thin films on a 2-inch diameter $LaAlO_3$ substrate with a dielectric constant $\varepsilon_r \cong 23$. Even with the cryocooler, the HTS filters are significantly smaller than conventional filters. This size reduction is especially important in urban base stations where space comes at a premium.

Although sales of HTS cellular filters have been steady, there is some reluctance to adopt these systems for widespread use. Of course the necessity of cooling the filters adds to the cost. Another factor limiting their acceptance is the lack of long term data on the performance of cryocoolers. The cryocoolers must work reliably and maintain a fixed temperature for at least 5 years with no regular maintenance. In addition, the cryogenic packaging must maintain its integrity over that time scale so that there is no interruption of service due to a vacuum leak and subsequent cryogenic failure.

Another serious limitation of current HTS filters is their high power performance. Since even optimal HTS thin films have low-angle grain boundaries, they show a

significant increase in loss and inductance at high power. This power dependence is often blamed on the creation and motion of Josephson vortices at weak links in the material. However, no direct experimental evidence exists on the microscopic origin of nonlinearity, so the question remains open. Improved deposition techniques have produced HTS films with dramatically better power handling capability. However, the thin film geometries required to achieve a given electrical performance often introduce regions in the device where very large current densities must flow. For example, currents flowing through a flat strip must have very large current densities at the edges to screen out the self-induced magnetic field. These areas of the devices are quite susceptible to rf breakdown. New filter designs, which do not involve the flow of current along patterned edges, are being developed to overcome these geometrical limitations.

5.2 Sources of non-linearity

It is well known that the hole-doped cuprate superconductors have intrinsic nonlinearities due to their d-wave pairing state symmetry [1]. However, practical thin film materials display microwave nonlinearities which are several orders of magnitude larger than this limit [2]. This is due to the presence of many extrinsic sources of nonlinearity, such as grain boundary weak links [3], damage at patterned edges, heating [4], and possibly other phenomena [5]. The identification of these extrinsic sources is an important step in eliminating them from materials used to fabricate microwave devices. This chapter describes my attempt to image these local sources of nonlinearity.

Macroscopically, nonlinearities can be described in terms of a surface impedance $Z_s = R_s + iX_s$ which is dependent on the excitation level. Direct measurements of the

nonlinear surface resistance (R_s) and reactance (X_s) in high temperature superconductors have shown a wide variety of behavior, ranging from increases which are linear, quadratic, or stronger in rf magnetic field strength [6]. Other researchers have reported surface impedance values which initially decrease over a substantial range of field strength [7]. In the absence of a microscopic investigation of these dependencies, a variety of contradictory models have been developed to explain the results.

Measurements of harmonic generation have also been used to characterize superconducting nonlinearities [8,9]. Here too there are a variety of results, typically explained by weak links and current crowding at the edges of the material. Perhaps, the most sensitive experimental characterization of superconducting nonlinearity is through intermodulation distortion (IMD) of two nearby pure tones [1,3,4]. Intermodulation is also a practical measurement because it simulates the undesirable generation of ghost signals in a passive bandpass filter, for example. Because of the sensitivity and practicality of IMD measurements, the measurements I describe in this chapter are focused on this important quantity.

5.3 Experimental Arrangement

The experimental configuration I used is shown schematically in Fig 5.1. The superconducting resonator is installed in a cryogenic scanning microwave microscope [10, 11]. Two microwave synthesizers send cw tones at frequencies f_1 and f_2 into the device through isolators, amplifiers, and a combiner. The response of the sample is detected in a spatially resolved manner through the scanned open-ended coaxial probe, as I described in Chapter 3. We used a coaxial cable probe with a center conductor diameter d_c= 200 μm

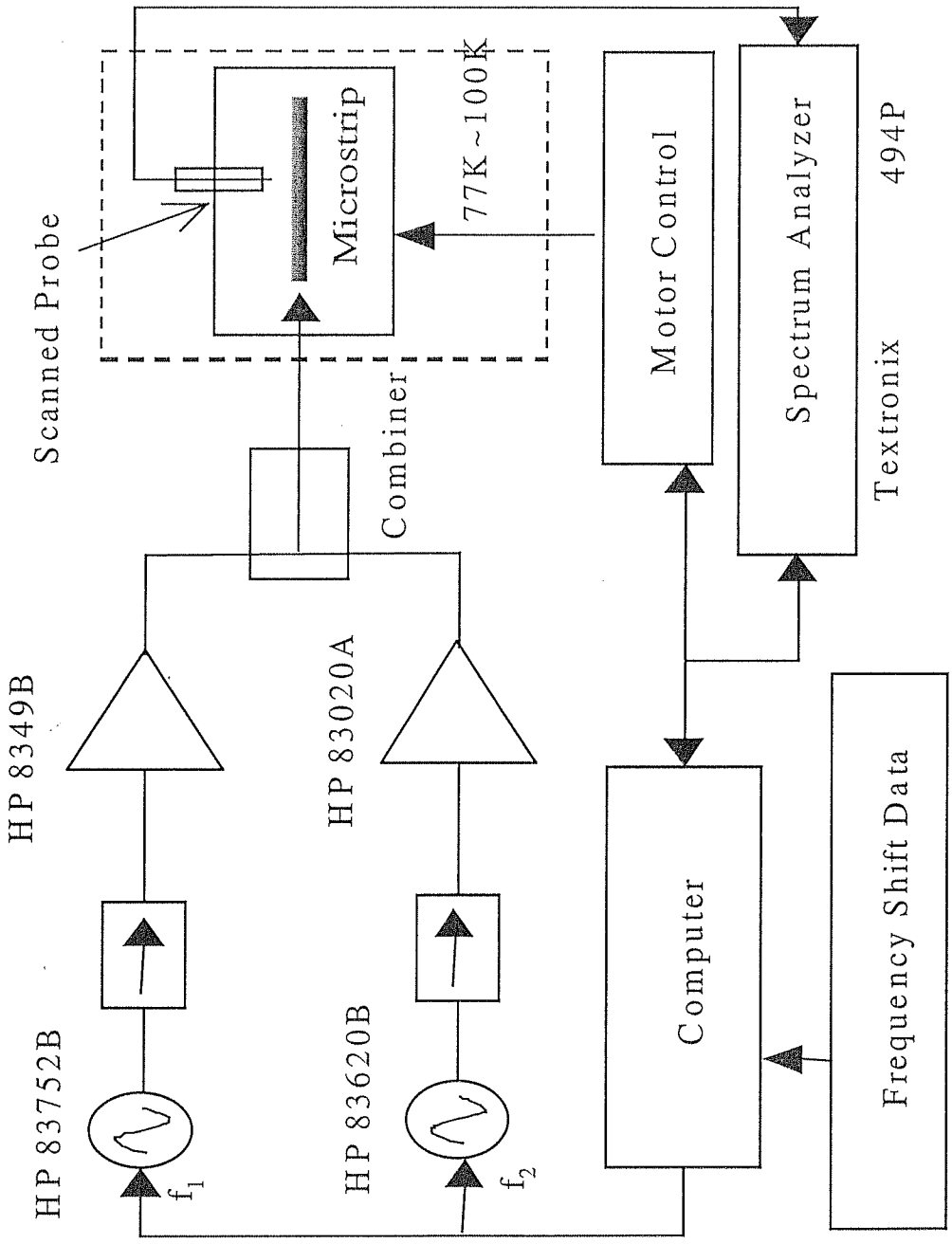

Fig. 5.1. Schematic of the microwave intermodulation experiment. The two sources provide signals to the device, while the scanned open-ended coaxial probe picks up the vertical component of the electric field. The collected power at different frequencies is selectively detected by the spectrum analyzer.

and an outer conductor diameter d_0 = 860 μm [12]. During a scan, the probe is held at a constant height h above the sample, typically between 10 μm and several millimeters. The electric field above the sample induces a high frequency potential difference between the center and grounded outer conductors of the probe. The probe is connected to a spectrum analyzer which can selectively measure the power at the linear response frequencies f_1 and f_2, or at the nearby third order IMD frequencies $2f_1$-f_2 and $2f_2$ - f_1. We use a computer to record the response at these four different frequencies and also control a two-axis translation stage, which raster scans the sample underneath the probe.

5.4 Test filter samples

For realistic testing of this technique, I imaged a 650 nm $Tl_2Ba_2CaCu_2O_8$ thin film microstrip resonator that was deposited on an MgO substrate. This filter was made by STI, Inc., and is the same one I described in Chapter 3. The microstrip has a T_c of 103 K and a fundamental resonant frequency at 77 K of approximately 8.2 GHz. [10]. The filter is 7.1 mm long, 150 μm wide and is mounted in a copper box with SMA connectors at each end (see Fig. 5.1). The top of the box is open to allow the coaxial probe to scan the surface.

5.5 Global Intermodulation

Before imaging Wensheng took some global measurement on the sample, i.e. we measured the response of the filter when signal was applied to the connectors. Figure 5.2 shows the results of such 9 standard "global" intermodulation measurement.

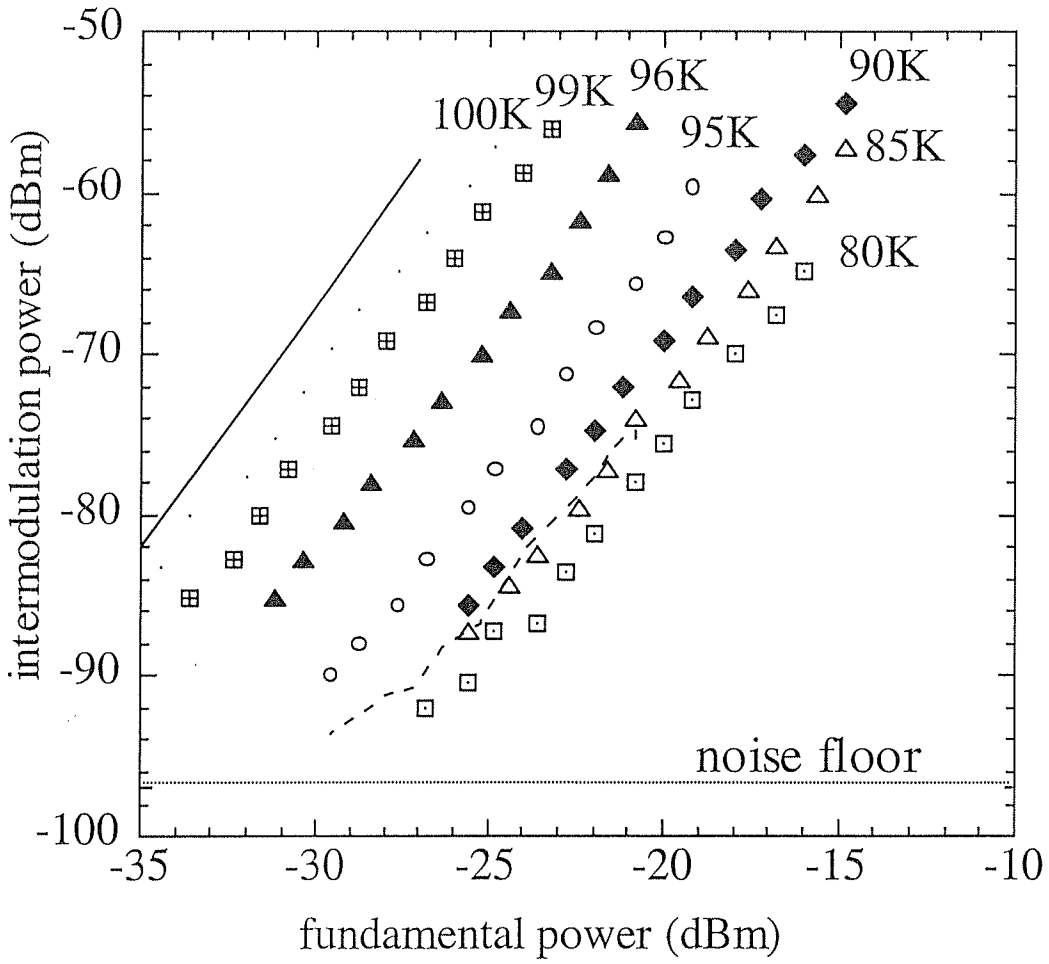

Fig. 5.2. Global intermodulation ($2f_1 - f_2$) power measured at the open end of the microstrip at a height of 200 μm vs. the measured power at the fundamental frequency f_1 = 8.2 GHz, at several temperatures. Also shown is 85 K data (dashed line) from the line cut of an image taken at a height of 200 μm, plotted in the same manner as the global data. Solid line shows cubic dependence of IMD on fundamental power.

For this plot, the probe was positioned over the end of the resonator opposite the drive pin, and the response was measured as a function of temperature and input power. The two tones are chosen to be 100 kHz apart to avoid the phase noise of the synthesizers at small frequency separations, and to remain within the middle of the passband of the resonator at 8.2 GHz (Q ~ 700-1400, depending on temperature).

We see from Fig. 5.2 that the IMD power increases roughly as the cube of the incident microwave power. This is what one expects for intermodulation, i.e. ideally one expects that third-order IMD power will increase three times faster than the incident power [13]. This is because a third-order non-linearity is the first non-zero term in the Taylor series expansion of the current-voltage (I-V) curve in time-reversal symmetric nonlinear systems. In practice, however, the situation is more complicated, and deviations are frequently seen, as at low powers in Fig. 5.2 [14, 15].

Figure 5.2 also shows that the IMD power grows as the transition temperature is approached from below. The point where the fundamental power intersects the intermodulation power is called the third-order intercept. By extrapolating the data in Fig. 5.2 we find that the approximate third-order intercept power decreases from +39 dBm at 80 K to +31 dBm at 99 K, indicating that nonlinearities grow stronger as the superfluid density diminishes (See figure 5.3).

5.6 Imaging intermodulation.

We next imaged the microwave fields above the device while applying two cw tones at +16 dBm which were 100 kHz apart and centered on the fundamental resonant frequency. To accomplish this, we had to account for perturbation of the fundamental

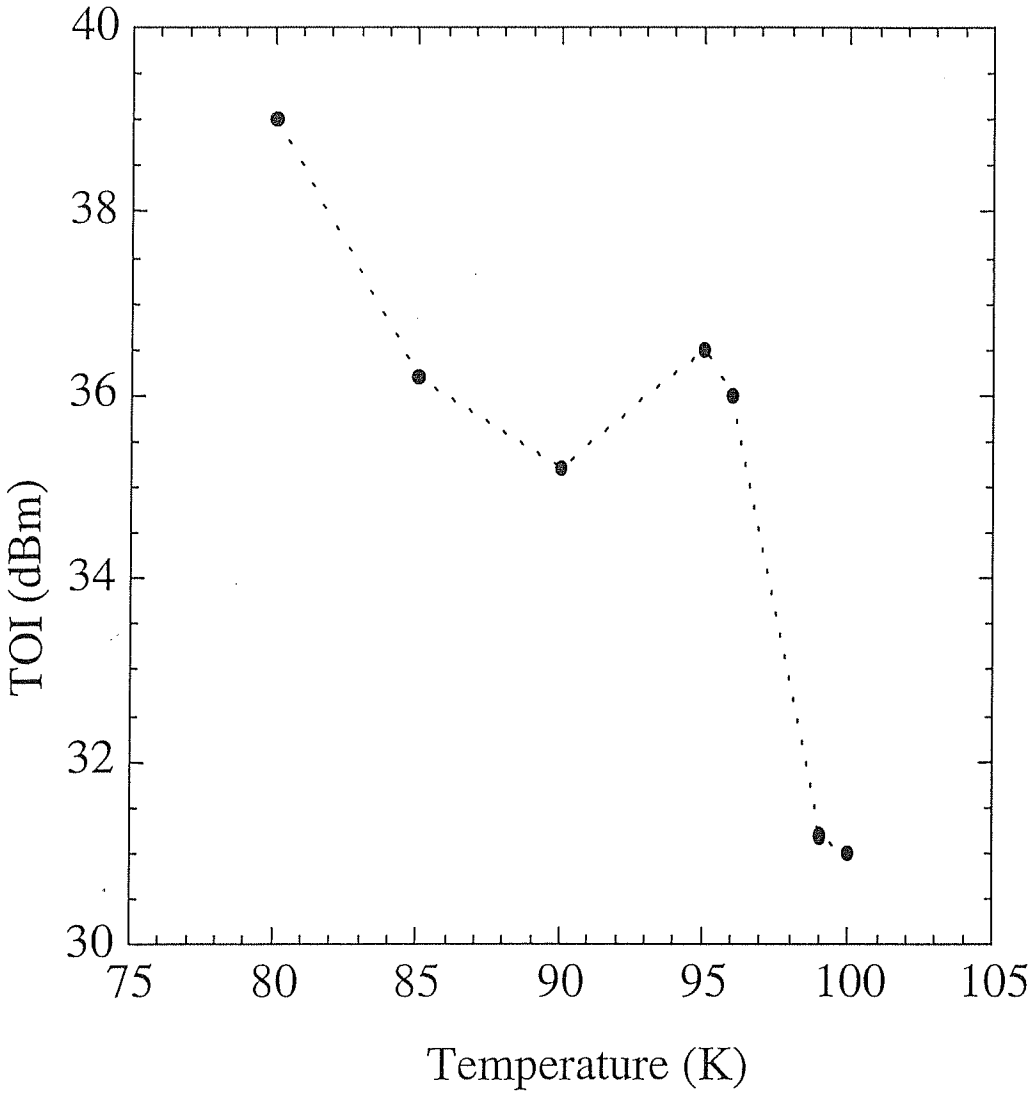

Fig. 5.3 The third order intercept power in dBm vs. the temperature T

resonant frequency of the device due to the probe [11]. Consequently, we first scanned the region of interest, recording the resonant frequency of the microstrip as a function of the position of the probe. Then we scanned the same region again, using the resonant frequency data to align the two tones so that they were centered within the passband of the device at each probe location. Figure 5.4 shows the resulting images of detected power versus position above the microstrip resonator at both the applied frequency f_1 and the intermodulation frequency $2f_1 - f_2$. The f_1 image [Fig. 5.4(a)] is similar to our previous results on this resonator [10], although the present image shows significantly greater dynamic range because of the use of a spectrum analyzer, rather than a diode, as a detector. The peak signals at either end of the resonator, and the minimum at the center, are consistent with a probe which detects power from just the z component of electric field in the fundamental standing wave pattern of this resonator [10, 12].

Figure 5.4(b) shows the intermodulation power versus position measured at the same time as the response at f_1. The IMD signal is smaller in amplitude but has a similar distribution in space. Upon closer inspection, however, one notes that the IMD image shows larger variations in power with position. This can be seen by taking longitudinal line cuts through the images in Fig. 5.4, as shown in Fig. 5.5. The response at f_1 fits qualitatively to a $\cos^2(\pi x/L)$ form, where x is the position along the resonator of length L, as expected for the fundamental standing wave [16]. In contrast, the intermodulation power is better fit to a $\cos^6(\pi x/L)$ form, showing that there is approximately a 3 to 1 ratio of IMD power to fundamental power point-by-point throughout the device.

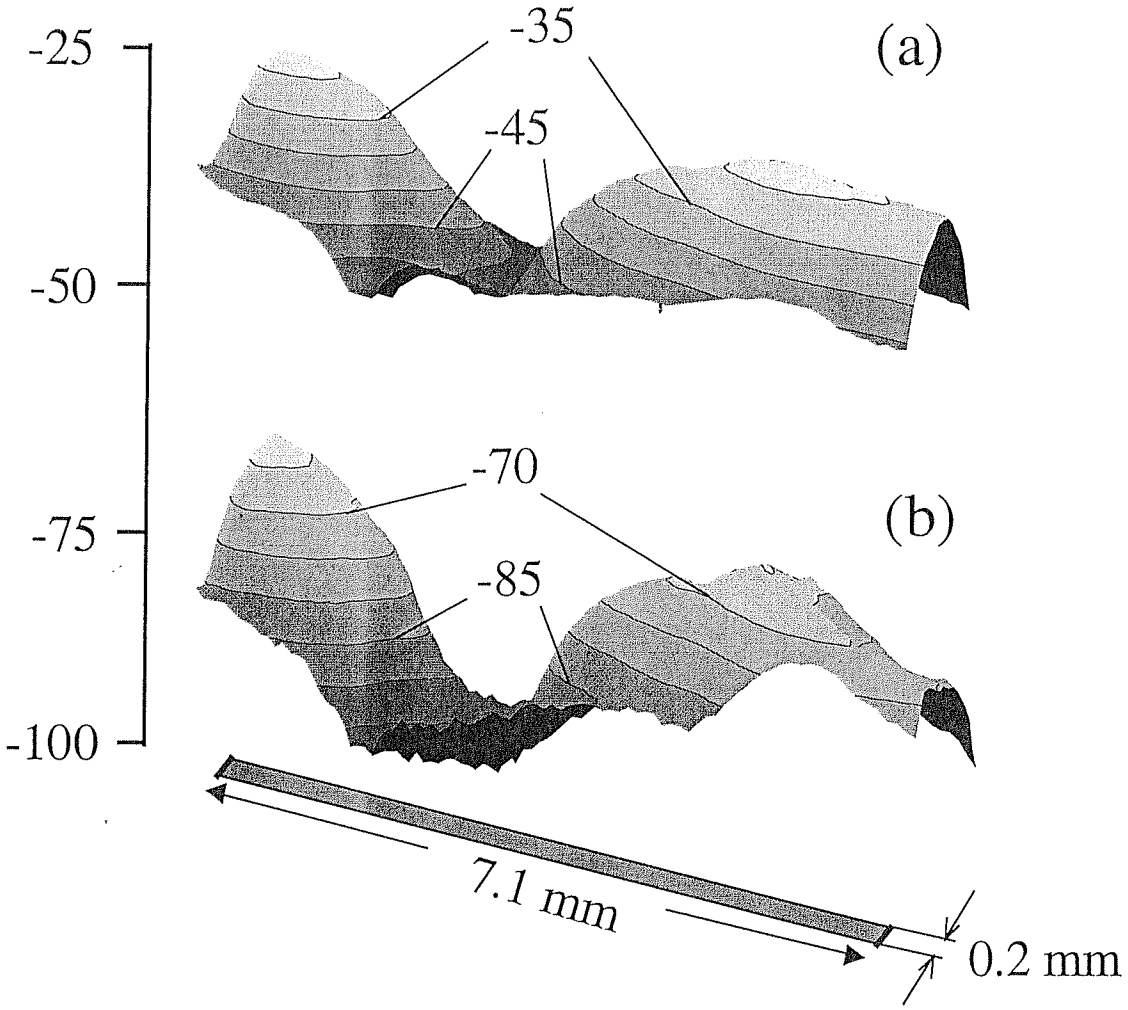

Fig. 5.4. Surface plots of (a) power at the fundamental frequency f_1 = 8.2 GHz of the superconducting resonator, and (b) intermodulation ($2f_1$-f_2) power, vs. position over the microstrip resonator at 96 K. The approximate location of the microstrip is shown as the shaded rectangle and the drive pin is on the left side. The input power is +16 dBm for both tones and the height of the probe is 550 μm.

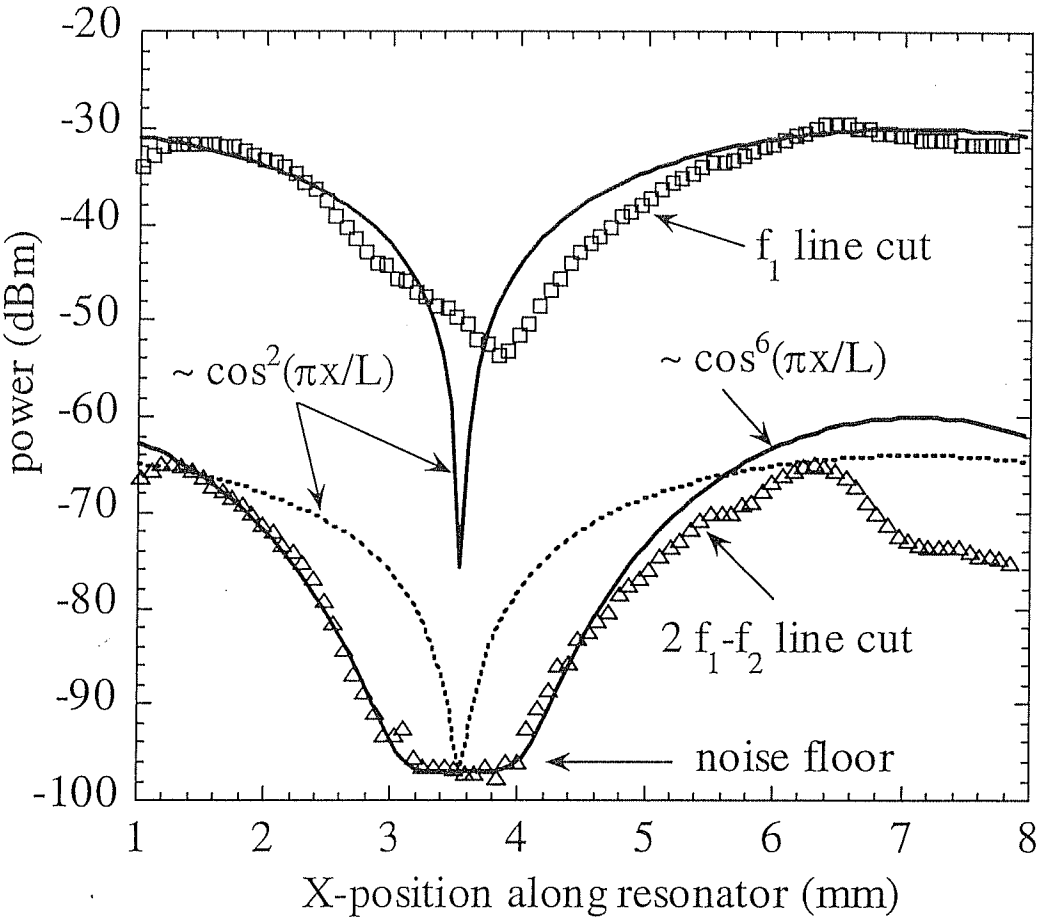

Fig. 5.5. Line cuts taken along the microstrip in Figs. 5.4 (a) and (b). The resonator extends from x = 0 to x = L = 7.1 mm. Also shown are fits to $\cos^2(\pi x/L)$ (fundamental) and $\cos^6(x/L)$ (IMD).

5.7 Discussion

Further insight into the distribution of IMD power in the resonator can be gained by plotting line cuts of fundamental and IMD images along side the global IMD data obtained by sweeping power. The dashed line and data points in Fig. 5.2 shows a comparison of these two entirely different methods of measuring IMD power at 85 K. The close agreement between these curves shows that the global IMD versus linear power information is present throughout the resonator. This suggests that information about local nonlinearities may be subsumed by the resonant nature of the IMD response.

The $\cos^6(\pi x/L)$ distribution of the IMD power is a well-known prediction of theories of intermodulation and third harmonic generation in superconducting resonators [1, 17]. However, existing treatments make the approximation that the IMD electric field is distributed as $E_{IMD} \sim \cos^3(\pi x/L) \simeq (3/4)\cos(\pi x/L)$, ignoring the $(1/4)\cos(3\pi x/L)$ term in the trigonometric identity. It is argued that the second term can be ignored because it will not propagate in the resonator since it has the wrong wavelength for the IMD frequency. However, our results clearly show that the IMD power distribution is very poorly described by a $P_{IMD} \sim |E_{IMD}|^2 \sim \cos^2(\pi x/L)$ term alone suggesting that our understanding of how IMD power is distributed in resonant systems may be incomplete.

We can simply model the intermodulation as being due to a microwave surface impedance which increases as $R_s(H_{rf}) = R_s(0)(1 + \alpha H^2_{rf})$ and $X_s(H_{rf}) = X_s(0)(1 + \beta H^2_{rf})$ [18]. Assuming that the reactance nonlinearity dominates [2], we can calculate the intermodulation levels following standard practices [14] and compare them to our measured IMD powers to determine the parameter β. The resulting values of $\beta(T/T_c) \sim 10^{-4}$ to 2×10^{-3} Oe^{-2} for $T/T_c = 0.78$ to 0.97 are in good agreement with those obtained by

Oates et al. from direct nonlinear surface impedance measurements on $YBa_2Cu_3O_7$ stripline resonators [18]. The fact that a quantitative weak link model was consistent with the stripline data [18] suggests a similar weak link origin for the nonlinearities observed here.

We believe that our IMD images represent the total standing wave pattern developed by the nonlinearities in the resonator, as opposed to an image of locally generated IMD. Because the nonlinearities are thought to arise from current dependence of the surface impedance, the IMD signals should be largest at the center of the resonator, where the current is highest. In fact, the opposite is true, which strongly suggests we are simply measuring the resonant response of the resonator rather the IMD source.

5.8 Conclusions

In conclusion, using a cryogenic near-field scanning microwave microscope, I have demonstrated frequency-selective imaging of electric fields generated by nonlinearities in a superconducting microstrip resonator. The intermodulation image shows that there is a simple relationship between the linear and nonlinear power levels at each location in the device and the levels are consistent with what one expects for superconductors having a modest nonlinearity in the surface impedance. Finally the results suggest that our understanding of the spatial distribution of intermodulation fields in resonant systems is incomplete.

I should note here that I have made other attempts at imaging localized sources of nonlinearity. In one approach, instead of applying two cw tones which are 100 KHz apart and centered on the fundamental resonant frequency of the device, I added a decoupler to

the probe to convert it into a resonant section and applied to it two cw tones which were 100 KHz apart and centered on the resonant frequency of the resonant section. The reflected signal was transmitted via a directional coupler to the spectrum analyzer. The idea was that this should produce a concentrated fundamental field which would only locally excite non-linear sources. Initially, the intermodulation power as recorded on the spectrum analyzer seemed to increase as the probe was brought closer to the sample (YBCO sample) in this case. However closer examination showed that this was not the case and in fact I was simply getting non-linear mixing from the analyzer itself. After I removed this by subtracting out the fundamental (using an additional feed from the source) the intermodulation disappeared. In the end, I concluded that although the idea seemed promising, I could not get enough power at the sample to excite non-linearities.

BIBLIOGRAPHY

Chapter 1

[1] J. G. Bednorz and K. A. Muller, Z. Phys. B **64**, 189 (1986).

[2] M. J. Scharen, D. R. Chase, A. M. Ho, A. O'Baid, K. R. Raihn and R. J. Forse, IEEE Trans. Appl. Supercon. **7**, 3744 (1997).

[3] R. Hammond, Hey-Shipton and G. Matthaei, IEEE Spectrum, April (1993).

[4] O. G. Vendik and I. B. Vendik, IEEE Trans. Microwave Theory Tech., **46**, 851 (1998).

[5] Zhengxiang Ma, E. de Obaldia, G. Hampel, P. Polakos, P. Mankiewich, B. Batlogg, W. Prusseit, H. Kinder, A. Anderson, D. E. Oates, R. Ono, J. Beall, IEEE Trans. Appl. Supercond. **7**, 1911 (1997).

[6] Z.-Y. Shen, *High-Temperature Superconducting Microwave Circuits* (Artech House, Boston, 1994).

[7] A. M. Portis, "*Electrodynamics of High-Temperature Superconductors*" (World Scientific Publishing Co., Singapore, 1993).

[8] E. Abbe, Archiv. Mikroskopische Anat. **9**, 413 (1873).

[9] E. H. Synge, Philos. Mag. **6**, 356 (1928).

[10] G. Binnig, H. Roher, Ch. Gerber, E. Weibel. Phys. Rev. Lett **49**, 57 (1982).

[11] C. Bohms, F. Saurenbach, P. Taschner, C. Roths and E. Kubaler, J. Phys. D, **26**, 1801 (1993).

[12] F. Giessible, Science **267**, 68 (1995).

[13] U. Durig, D. W. Pohl, F. Rohner, J. Appl. Phys. **59**, 3318 (1986).

[14] E. Betzig and J. K. Trautman, Science **257**, 189 (1992).

[15] Y. Martin and H. K. Wickramasinghe, Appl. Phys. Lett. **50**, 1455 (1987).

[16] P. C. D. Hobbs, D. W. Abraham, and H. K. Wickramasinghe, Appl. Phys. Lett. **55**, 2357 (1989).

[17] T. P. Budka, S. D. Waclawik, G. M. Rebeiz, IEEE Trans. MTT **44**, 2174 (1996).

[18] D. W. van der Weide, and P. Nuezil, J. Vac. Sci. Technol. B **14**, 4144 (1996).

[19] V. Agrawal, P. Nuezil, and D. van der Weide, Appl. Phys. Lett. **71**, 2343 (1997).

[20] T. Kaiser, M. A. Hein, G. Muller, and M. Perpeet, Appl. Phys. Lett. **73**, 3447 (1998).

[21] H. S. Newman, and J. C. Culbertson, Microwave Opt. Tech. Lett. **6**, 725 (1993).

[22] R. Gerber, et al., Appl. Phys. Lett. **66**, 1554 (1995).

Chapter 2

[1] A. Mathai, D. Song, Y. Gim, and F. C. Wellstood, *Appl. Phys. Lett.* **61**, 598 (1992).

[2] R. C. Black, A. Mathai, F. C. Wellstood, E. Dantsker, A. H. Miklich, and D. T. Nemeth, *Appl. Phys. Lett,* **62**, 2128 (1993).

[3] R. C. Black, *Magnetic microscopy using a superconducting quantum interference device,* Ph. D. Thesis, University of Maryland, College Park, Maryland, August 1995.

[4] F. C. Wellstood, Y. Gim, A. Amar, R. C. Black, and A. Mathai, *IEEE Trans. on Appl. Supercond.* **5**, 3233 (1995).

[5] R. C. Black, *Magnetic microscopy using a superconducting quantum interference device,* Ph. D. Thesis, University of Maryland, College Park, Maryland, August 1995.

[6] R. C. Black, F. C. Wellstood, E. Dantsker, A. H. Miklich, J. J. Kingston, D. T. Nemeth and J. Clarke, *Appl. Phys. Lett.* **64**, 100 (1994).

[7] A. Mathai, Y. Gim, R. C. Black, A. Amar and F. C. Wellstood, *Phys. Rev. Lett.* **74**, 4523 (1995).

[8] A. Mathai, Y. Gim, R. C. Black, A. Amar and F. C. Wellstood, *Journal of Superconductivity* **8**, 491 (1995).

[9] C. P. Vlahacos, R. C. Black, S. M. Anlage, A. Amar, and F. C. Wellstood, Appl. Phys. Lett. **69**, 3272 (1998).

[10] C. P. Vlahacos, D. E. Steinhauer, S. K. Dutta, B. J. Feenstra, Steven M. Anlage and F. C. Wellstood, *Appl. Phys. Lett.* **72**, 1778 (1998).

[11] B. J. Feenstra, C. P. Vlahacos, Ashfaq S. Thanawalla, D. E. Steinhauer, S. K. Dutta, F. C. Wellstood, and S. M. Anlage, *IEEE MTT-S Int. Microwave Symp. Dig.*, p. 965 (1998).

[12] D. E. Steinhauer, C. P. Vlahacos, S. K. Dutta, F. C. Wellstood, and Steven M. Anlage, *Appl. Phys. Lett.* **71**, 1736, 1997.

[13] D. E. Steinhauer, C. P. Vlahacos, S. K. Dutta, B. J. Feenstra, F. C. Wellstood, and Steven M. Anlage, *Appl. Phys. Lett.* **72**, 861, 1998.

[14] D. E. Steinhauer, *Quantitative imaging of sheet resistance, permittivity and ferroelectric critical phenomena with a near-field scanning microwave microscope,* Ph. D. Thesis, University of Maryland, College Park, Maryland, 2000.

[15] D. E. Steinhauer, C. P. Vlahacos, F. C. Wellstood, Steven M. Anlage, C. Canedy, R. Ramesh, A. Stanishevsky, and R. Ramesh, Appl. Phys. Lett. **75**, 3180, 1999.

[16] 8 wire, 1/4" shaft skew pole stepper motors from Eastern Air Devices, Dover, NH.

[17] MD10A Microstep Motor Drives and PC34-4 4-axis controller from Oregon Microsystems, Beaverton, OR.

[18] Model MPS28-07 (28 V, 7 A) power supply from Cyber Research, Brandford, CT.

[19] National Instruments Model AT-MIO-16X, 16 bit, 16 analog input channel A/D board.

Chapter 3

[1] M. J. Scharen, D. R. Chase, A. M. Ho, A. O'Baid, K. R. Raihn and R. J. Forse, IEEE Trans.Appl. Supecond. **7**, 3744 (1997).

[2] Z.-Y. Shen, High-Temperasture Superconducting Microwave Circuits (Artech House, Boston, 1994).

[3] J. Halbritter, J. Appl. Phys. **68**, 6315 (1990); J. Halbritter, J. Supercond. **8**, 691 (1995).

[4] D. E. Oates, P. P. Nguyen, G. Dresselhaus, M. S. Dresselhaus, C. W. Lam, and S. M. Ali, J. Supercond. **5**, 361 (1992).

[5] G. Hampel, B. Batlogg, K. Krishana, N. P. Ong, W. Prusseit, H. Kinder, and A. C. Anderson, Appl. Phys. Lett. **71**, 3904 (1997).

[6] H. S. Newman and J. C. Culbertson, Microwave Opt. Technol. Lett. **6**, 725 (1993).

[7] R. C. Black, F. C. Wellstood, E. Dantsker, A. H. Miklich, D. Koelle, F. Ludwig, and J.Clarke, Appl. Phys. Lett. **66**, 1267 (1995).

[8] G. Hampel, P. Kolodner, P. L. Gammel, P. A. Polakos, E. De Obaldia, P. M. Mankiewich, A. Anderson, R. Slattery, D. Zhang, G. C. Liang, and C. F.Shih, Appl. Phys. Lett. **69**, 571 (1996).

[9] J. Gallop, L. Hao, and F. Abbas, Physica C **282-287**, 1579 (1997).

[10] T. P. Budka, S. D. Waclawik, and G. M. Rebeiz, IEEE Trans. Microwave Theory Tech. **44**, 2174 (1996).

[11] K. J. Weingarten, M. J. W. Rodwell, and D. M. Bloom, IEEE J. Quantum Electron. 24, 198 (1998), and references therein.

[12] A. S. Hou, F. Ho and D. M. Bloom, Electron. Lett. **28**, 2302 (1992).

[13] D. W. van der Weide and P. Neuzil, J. Vac. Sci. Technol. B **14**, 4144 (1996).

[14] Ashfaq S. Thanawalla, S. K. Dutta, C. P. Vlahacos, D. E. Steinhauer, B. J. Feenstra, Steven M. Anlage, F. C. Wellstood and Robert B. Hammond, Appl. Phys. Lett. **73**, 2491 (1998).

[15] S. M. Anlage, C. P. Vlahacos, S. K. Dutta, and F. C. Wellstood, IEEE Trans. Appl. Supercond. **7**, 3686 (1997).

[16] B. J. Feenstra, C. P. Vlahacos, Ashfaq S. Thanawalla, D.E. Steinhauer, S. K. Dutta, F. C. Wellstood, and S. M. Anlage, IEEE MTT-S Int. Microwave Symp. Dig. **46**, 965 (1998).

[17] Superconductor Technology, Inc., sample TM0171- R_1, R_2, R_3.

[18] One expects the BCS temperature dependence to be obeyed for a d-wave superconductor near T_c, in the absence of critical fluctuations.

[19] B. A. Willemsen, K. E. Kihlstrom, T. Dahm, D. J. Scalapino, B. Gowe, D. A. Bonn, and W. N. Hardy, Phys. Rev. B **58**, 6650 (1998).

[20] D.E. Steinhauer, C. P. Vlahacos, S. K. Dutta, F. C. Wellstood, and S. M. Anlage, Appl. Phys. Lett. **71**, 1736 (1997).

Chapter 4

[1] D. E. Steinhauer, C. P. Vlahacos, S. K. Dutta, F. C. Wellstood, and Steven M. Anlage, Appl. Phys. Lett. **71**, 1736 (1997).

[2] L. C. Maier, and J. C. Slater, J. Appl. Phys. **23**, 68 (1952).

Chapter 5

[1] T. Dahm and D. J. Scalapino, Appl. Phys. Lett. **69**, 4248 (1996).

[2] R. B. Hammond, E. R. Soares, B. A. Willemsen, T. Dahm, D. J. Scalapino, and J. R. Schrieffer, J. Appl. Phys. **84**, 5662 (1998).

[3] T. C. Sollner, J. P. Sage, and D. E. Oates, Appl. Phys. Lett. **68**, 1003 (1996).

[4] W. Diete, M. Getta, M. Hein, T. Kaiser, G. Muller, H. Piel, and H. Schlick, IEEE Trans. Appl. Supercond. **7**, 1236 (1997).

[5] M. Golosovsky, Supercond. Sci. Technol. **9**, 1 (1996).

[6] P. P. Nguyen, D. E. Oates, G. Dresselhaus, and M. S. Dresselhaus, Phys. Rev. B **48**, 6400 (1993).

[7] M. A. Hein, C. Bauer, W. Diete, S. Hensen, T. Kaiser, V. Z. Kresin, and G. Muller, J. Supercond. **10**, 485 (1997).

[8] C. Wilker, Z. Y. Shen, P. Pang, W. L Holstein, and D. W. Face, IEEE Trans. Appl. Supercond. **5**, 1665 (1995).

[9] G. Hampel, B. Batlogg, K. Krishana, N. P. Ong, W. Prusseit, H. Kinder, and A. C. Anderson, Appl. Phys. Lett. **71**, 3904 (1997).

[10] Ashfaq S. Thanawalla, S. K. Dutta, C. P. Vlahacos, D. E. Steinhauer, B. J. Feenstra, S. M. Anlage, F. C. Wellstood, and R. B. Hammond, Appl. Phys. Lett. **73**, 2491 (1998).

[11] Ashfaq S. Thanawalla, W. Hu, D. E. Steinhauer, S. K. Dutta, B. J. Feenstra, S. M.

Anlage, F. C. Wellstood, and R. B. Hammond, IEEE Trans. Appl. Supercond. **9**, 3042 (1999).

[12] S. K. Dutta, C. P. Vlahacos, D. E. Steinhauer, Ashfaq S.Thanawalla, B. J. Feenstra, F. C. Wellstood, S. M. Anlage, and H. S. Newman, Appl. Phys. Lett. **74**, 156 (1999).

[13] Z. Y. Shen, *High-Temperatue Superconducting Microwave Circuits* (Artech, Boston, 1994), p. 47.

[14] S. K. Remillard, L. J. Klemptner, J.D. Hodge, T. A. Freeman, P. A. Smith, and T. W. Button, Proc. SPIE, **2559**, 59, 1995.

[15] B. A. Willemsen, K. E. Kihlstrom, and T. Dahm, Appl. Phys. Lett. **74**, 753 (1999).

[16] The spatial resolution of the microscope is limited to the probe-sample separation (550 μm) in this case, hence the dip in fundamental power at the center of the resonator is not resolved in Fig. 5.4.

[17] O. G. Vendik, I. B. Vendik, and T. B. Samoilova, IEEE Trans, Microwave Theory Tech. 45, 173 (1997).

[18] D. E. Oates, P. P. Nguyen, G.Dresselhaus, M. S. Dresselhaus, and C. C. Chin, IEEE Trans. Appl. Supercond. **3**, 1114 (1993).